A&A 441, 181–194 (2005)
DOI: 10.1051/0004-6361:20042149

Astronomy & Astrophysics

Interstellar $^{12}C/^{13}C$ ratios through $CH^+ \lambda\lambda 3957,4232$ absorption in local clouds: incomplete mixing in the ISM⋆,⋆⋆,⋆⋆⋆

S. Casassus[1], O. Stahl[2], and T. L. Wilson[3,4]

[1] Departamento de Astronomía, Universidad de Chile, Casilla 36-D, Santiago, Chile
e-mail: simon@das.uchile.cl
[2] Landessternwarte Königstuhl, 69117 Heidelberg, Germany
e-mail: O.Stahl@lsw.uni-heidelberg.de
[3] ESO, Karl-Schwarzschild-Str. 2, 85748 Garching bei München, Germany
e-mail: twilson@eso.org
[4] Max-Planck-Institut für Radioastronomie, Postfach 2024, 53010 Bonn, Germany

Received 8 October 2004 / Accepted 2 June 2005

Abstract. The $^{12}C/^{13}C$ isotope ratio is a tracer of stellar yields and the efficiency of mixing in the ISM. $^{12}CH^+/^{13}CH^+$ is not affected by interstellar chemistry, and is the most secure way of measuring $^{12}C/^{13}C$ in the diffuse ISM. $R = {}^{12}C/{}^{13}C$ is 90 in the solar system. Previous measurements of $^{12}CH^+ \lambda\lambda 3957.7,4232.3$ and $^{13}CH^+ \lambda\lambda 3958.2,4232.0$ absorption toward nearby stars indicate some variations in $^{12}C/^{13}C$, with values ranging from 40 to 90 suggesting inefficient mixing. Except for the cloud toward ζOph, these R values are strongly affected by noise. With UVES on the VLT we have improved on the previous interstellar $^{12}C/^{13}C$ measurements. The weighted $^{12}C/^{13}C$ ratio in the local ISM is 78.27 ± 1.83, while the weighted dispersion of our measurements is 12.7, giving a 6.9σ scatter. Thus we report on a 6.9σ detection of 16.2% root-mean-square variations in the carbon isotopic ratio on scales of ∼100 pc: $R = 74.7 \pm 2.3$ in the ζOph cloud, while $R = 88.6 \pm 3.0$ toward HD 152235 in the Lupus clouds, $R = 62.2 \pm 5.3$ towards HD 110432 in the Coalsack, and $R = 98.9 \pm 10.1$ toward HD 170740. The observed variations in $^{13}C/^{12}C$ are the first significant detection of chemical heterogeneity in the local ISM.

Key words. ISM: abundances – ISM: clouds – ISM: molecules – ISM: individual objects: Coalsack – ISM: individual objects: Lupus cloud – ISM: individual objects: ζOph cloud

1. Introduction

The ratio of the ^{12}C to ^{13}C isotope is a good tracer of the amount of stellar processing in low and intermediate mass stars during the asymptotic giant branch (AGB) phase. The third dredge-up increases $^{12}C/^{13}C$ to about ∼300, while stars massive enough to undergo "hot bottom burning" bring their surface carbon isotopic ratio to CNO processing equilibrium, $^{12}C/^{13}C \sim 3$. The carbon yields of AGB stars are sensitive functions of their initial masses and metallicities (e.g. Renzini & Voli 1981; or Casassus & Roche 2001, for a population synthesis approach and references to model results).

A measurement of the $^{12}C/^{13}C$ ratio in the interstellar medium (ISM) gives important data for the total amount of low mass stellar evolution and subsequent enrichment of the ISM in the Galaxy. The terrestrial value of $^{12}C/^{13}C$ is 90 (Rosman & Taylor 1998). The $^{12}C/^{13}C$ ratio is a cornerstone of models of the nuclear history of our galactic ISM, that is, the Galactic Chemical Evolution. Models of chemical evolution predict a decrease in the $^{12}C/^{13}C$ ratio with time for a given galactocentric distance, and a decrease with galactocentric distance in the Galaxy (e.g. Palla et al. 2000, their Figs. 4 and 5.). Such models use the assumption that mixing in the ISM is complete and restricted to material at a given galactocentric distance (azimuthal mixing). A comparison of results between our Galaxy and other galaxies will give important data for the nuclear processing history (see, e.g., Tosi 2000; Prantzos 2001).

There are a large number of measurements of the $^{12}C/^{13}C$ ratio from radio astronomy data (see, e.g., Wilson & Rood 1994). However, these results may be affected by interstellar chemistry in two ways. These are chemical fractionation (which enriches molecules in ^{13}C and thus lowers the ratio) and selective dissociation (which destroys the rarer species more,

⋆ Based on observations obtained with UVES at the ESO Very Large Telescope, Paranal, Chile (proposal No. 71.C-0367(A)).
⋆⋆ Complete Figs. 3–5, 10–12 are available at http://www.edpsciences.org
⋆⋆⋆ The reduced spectra in fits format are available in electronic form at the CDS via anonymous ftp to cdsarc.u-strasbg.fr (130.79.128.5) or via http://cdsweb.u-strasbg.fr/cgi-bin/qcat?J/A+A/441/181

and thus raises the ratio). The ^{13}C enrichment is due to fractionation of the CO molecule via the ion-molecule process,

$$^{13}C^+ + {}^{12}CO \overset{k}{\rightleftharpoons} {}^{12}C^+ + {}^{13}CO + \Delta E, \quad (1)$$

with $\Delta E/k = 35$ K and $k = 2\times10^{-10}$ cm^3 s^{-1} in both directions (Watson et al. 1976). If the reaction reaches equilibrium,

$$\frac{n(^{13}C^+)\, n(^{12}CO)}{n(^{12}C^+)\, n(^{13}CO)} = \exp\left(-\frac{\Delta E}{kT}\right). \quad (2)$$

In cold gas, with $T \lesssim 35$ K, CO will be enriched in ^{13}C compared to C^+. The effect is observed in CO absorption towards ζOph (Sheffer et al. 1992), ρOph and χOph (Federman et al. 2003). Thus molecules whose synthesis involve CO at a later stage than C^+ will show the CO fractionation, and vice-versa (e.g. Watson 1978). The corresponding ^{13}C depletion in C^+ is diluted in environments where $n(C^+) \gg n(CO)$, such as diffuse clouds or photo-dissocitation regions (PDRs) at $A_V < 2$ (e.g. Keene et al. 1998, their Fig. 2).

Ultra-high-resolution spectroscopy of CH^+ (Crawford et al. 1994) absorption towards ζOph reveals broader profiles compared to CN and CH, with an upper limit kinetic temperature of ~2000 K, and with no velocity offset. This is consistent with CH^+ production through the endothermic reaction

$$C^+ + H_2 + 0.4\ \text{eV} \rightarrow CH^+ + H. \quad (3)$$

The analog of Eq. (2) shows that temperatures > 1000 K are required for CH^+ production via Eq. (3). CH^+ thus arises in the warm halo, or photo-dissociation region, surrounding the ζOph cloud. Crawford (1995) and Crane et al. (1991) extend the ζOph results to five and twenty other lines of sight through translucent clouds (i.e. with $A_V < 2$). With such a kinetic temperature, it is clear that CO fractionation in the sites of CH^+ production is negligible.

The carbon isotope ratio as measured by $^{12}CH^+/^{13}CH^+$ is not affected by selective dissociation. Although photodissociation of CH^+ contributes to PDR chemical networks (Sternberg & Dalgarno 1992), CH^+ is optically thin to photodissociating UV radiation in translucent clouds. The strongest optical CH^+ line in ζOph is $A^1\Pi - X^1\Sigma^+$ at 4232 Å (Morton 1975), which reaches maximum opacities of ~0.3 (e.g. this work). Since no ultra-violet CH^+ lines have been reported, they are bound to be faint, and thus thin. The photodissociation cross-section $\sigma(\nu)$ calculated by Kirby et al. (1980) is mostly due to transitions from the ground $X^1\Sigma^+$ state to the vibrational continua of the $2^1\Sigma^+$, $3^1\Sigma^+$, and $2^1\Pi$ states, which smooths out any difference between isotopes. Some resonant absorption derives from the calculation of $\sigma(\lambda)$ at wavelengths of 1418 Å, 1453 Å, and 1490 Å. But Kirby et al. (1980) assign oscillator strengths of less than 10^{-3} in any of these peaks, which represents Einstein B absorption rates one order of magnitude smaller than at 4232 Å.

The $^{12}CH^+/^{13}CH^+$ ratio is thus a secure representation of $^{12}C/^{13}C$ in translucent clouds. In addition, the absorption line from $^{12}CH^+$ at 4232 Å is separated from the line of $^{13}CH^+$ by 0.265 Å, which permits unblended measurements. These ratios, obtained from optical measurements, are restricted to regions within ~2 kpc of the Sun because of the need for bright background stars, and of narrow velocity profiles in the intervening cloud. Eight ratios have been measured but only one line of sight, toward ζOph, has an excellent signal to noise ratio. The average $^{12}C/^{13}C$ ratio from CH^+ data agrees well with those obtained for sources near the Sun, from radio astronomy data. This gives one confidence in the ratios obtained from radio data.

However, the CH^+ measurements so far resulted in isotopic ratios with a large scatter between different lines of sight, and there is only one line of sight with an excellent signal to noise ratio. The previous data from CH^+ were taken with the ESO CAT, and 4-m or smaller aperture telescopes. The best results from the point of view of the signal to noise ratio and the reliability of the ratio for ζOph were presented by 3 different groups (Stahl et al. 1989; Stahl & Wilson 1992; Crane et al. 1991; Hawkins et al. 1985, 1993). The final ratio obtained by each group was 67 ± 5. The ζOph value is by far the best measurement of the $^{12}C/^{13}C$ ratio for the ISM near the Sun. However, the measurements for 7 other nearby weak sources were of lower quality. The ratios for 3 of these regions, toward HD 26676 (64 ± 6, Centurion & Vladilo 1991), HD 110432 (71 ± 11, Centurion et al. 1995), and μNorma (67 ± 6, Centurion & Vladilo 1991) are in very good agreement with the ζOph ratio. But there are discordant ratios: $R = 38 \pm 12$ toward HD 157038 (Hawkins & Meyer 1989), and $R = 49 \pm 15$ toward ζPer (Hawkins et al. 1993) while the ratio toward HD 152235 is $R = 126 \pm 29$ and is $R = 98 \pm 19$ towards HD 152424 (Vladilo et al. 1993). Most of the measurements are limited by noise, but the profile toward HD 152424 is complex and thus a determination of the ratio is not easy, because of CH^+ and $^{13}CH^+$ line blending.

We repeated the CH^+ observations toward ζOph, HD 110432, HD 152235, HD 152424 and HD 157038, and included the new lines of sight toward HD 152236, HD 154368, HD 161056, HD 169454, HD 170740. Our goal was first to determine whether the ratios are truly different from the value for ζOph, which would indicate that the mixing of the ISM is not very fast and complete, and second, we wanted to increase the sample of lines of sight with good to excellent signal to noise ratios, and from this determine an average ratio near the Sun truly representative for the local ISM.

Section 2 describes the observations, and Sect. 3 gives details on our procedure to measure the isotopic ratio R. Section 4 contains our results, which are then summarised and discussed in Sect. 5. Section 6 concludes.

2. Observations and reduction

There are two systems of CH^+ lines which have appreciable oscillator strengths. Because of atmospheric absorption, the lines at 4232 Å are easier to measure. The $^{13}CH^+$ line is 0.26 Å ($\Delta v = 19$ km s^{-1}) shortward of the $^{12}CH^+$ line. The other system, at 3957 Å, is more difficult to measure, but has the property that the $^{13}CH^+$ line is on the long wavelength side of the $^{12}CH^+$ line at a separation of 0.44 Å ($\Delta v = -33$ km s^{-1}). This property has been used by Stahl & Wilson (1992) to check that there is no accidental overlap of a weak velocity component

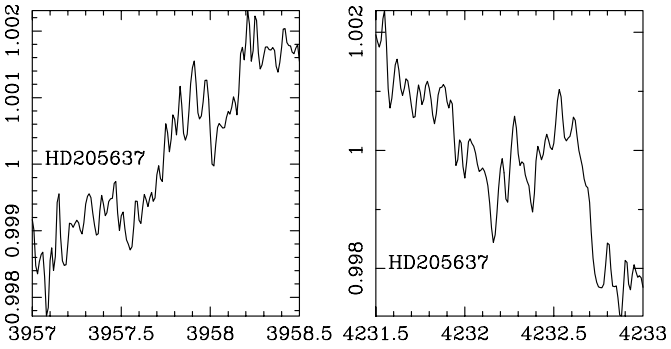

Fig. 1. Spectral region about the CH^+ absorption towards the template star HD 205637, emphasizing the absence of telluric features at airmasses of 1.05–1.08.

of $^{12}CH^+$ at -18.8 km s^{-1} from the deepest $^{12}CH^+$ absorption line with the $^{13}CH^+$ line. Nearly all previous data were taken at 4232 Å.

Our observations were obtained with the UVES echelle spectrograph at the VLT unit telescope Kueyen at Cerro Paranal, Chile, in three nights between June 14/15 and June 16/17, 2003. UVES allows measuring both line systems in the same detector setting, thus providing a means to correct for line blending if it is apparent in the spectra.

The observations are difficult because of the need for both very high S/N and very high spectral resolution to acquire the profile of faint $^{13}CH^+$, against a very bright stellar continuum and close to the much stronger $^{12}CH^+$ component. We need S/N ratios of at least ∼10 on $^{13}CH^+$ for accurate profile fitting. The project requires the highest possible spectral resolution. We therefore used an image slicer to minimize flux losses. In addition, the image slicer distributes the light along the slit, which improves flat-fielding and allows for our bright targets longer integration times before saturation occurs. UVES slicer #2 was used, which reformats an entrance opening of 1.″8 × 2.″2 to a slit of 0.″44 width and a length of 7.″9, which is imaged on the spectrograph entrance slit of 0.″45 width. The spectral resolution in this configuration is $\lambda/\Delta\lambda = 75\,000$. The central wavelength was set to 4370 Å, which gives a spectral coverage from 3730 to 5000 Å. During our observations the seeing was typically too good to fill the entrance aperture of the images slicer. Therefore, for most spectra, only one or two slices contained most of the signal, which unfortunately decreases the expected gain of the image slicer.

Accurate flat-fielding is also important. Therefore a large number of flat-fields (200) was obtained during daytime distributed along the observing run.

In addition, a rapidly rotating unreddened early-type star (ε Cap = HD 205637, spectral type B3V) was observed in order to check for possible faint terrestrial features. We confirm there are no detectable telluric features under the CH^+ absorption, and show in Fig. 1 the template star spectrum in the region of interest, at airmasses <1.08. Higher airmasses result in telluric absorption features, as in the case of ζOph discussed below.

The brighter targets where exposed until about 50% of the maximum level allowed by the CCD detector was reached. For ζ Oph, this limits the exposure time to about 5 s, and typically a few minutes for the fainter targets. Series of up to 50 exposures per night were obtained to build up the required S/N-ratio. Some targets turned out to show too complex line profiles. These were dropped from our initial target list. The observations are summarized in Table 1, which also lists the mean airmass of the target objects in the different nights. At the higher airmass values, the range in airmass differed from the mean by about ±0.1 during the observations, and less at smaller airmass.

Table 1. Summary of the observations, giving the total number of exposures, N, the integrated exposure time in seconds, and the observed heliocentric velocities of the absorbing clouds, $V_\odot$.

Object	Air mass			N	Exp.	$V_\odot$
	14/06	15/06	16/06		time	km s^{-1}
ζ Oph	1.16	1.81	1.71	150	750	–15.1
HD 110432	1.31	1.29	1.29	72	6770	+5.1
HD 152235	1.07	1.31	1.24	65	16 250	–4.3
HD 152236	–	1.14	–	10	600	–6.9
HD 152424	1.05	–	–	10	2500	–7.6
HD 154368	1.05	1.06	1.05	50	9850	–6.0
HD 157038	1.11	–	–	10	2500	–14.7
HD 161056	1.25	1.06	1.06	59	11 110	–11.4
HD 169454	1.30	1.12	1.12	50	22 900	–10.5
HD 170740	1.05	1.62	1.60	65	7800	–11.0
HD 205637	1.05	1.08	1.08	150	3385	–

We also list in Table 1 the radial velocities relative to the solar barycentre of the CH^+ absorption. These are calculated from the shift in wavelength between the rest wavelengths of the transitions and of the average of the Gaussian centroids weighted by their equivalent widths. The uncertainty on the derived velocities is conservatively ∼1 km s^{-1}, and depends on the accuracy of the rest wavelengths.

We used the Midas package originally developed for the ESO Feros spectrograph for the reduction of the spectra (Stahl et al. 1999). In order to maximize the S/N-ratio of the extracted spectra, all flat-fields obtained during the run were averaged. After background subtraction and flat-fielding, the spectra were extracted with a very long slit, extracting all slices together. The wavelength calibration of the extracted spectra was done with a 2D-polynomial, fitting all echelle orders in one step. A mean ThAr-spectrum obtained during day time was used for the calibration of all spectra obtained in one night. Finally, all spectra were merged to a 1D-spectrum and all observations of each night averaged to a nightly mean spectrum. Wavelengths are reported in air and refererred to the solar barycentre.

The nightly spectra were combined in a weighted average to produce coadded spectra. The weights were taken as $1/\sigma^2$, where σ is the noise in each spectra, as calculated from the root-mean-square deviations from a linear fit to a region of the spectrum devoid of conspicuous features (we chose 4204.2 Å to 4205.9 Å). Table 2 summarise the resulting weights.

Table 2. Relative weights used to combined the nightly spectra.

	June 14	June 15	June 16
ζOph	0.45	0.30	0.26
HD 110432	0.26	0.37	0.36
HD 152235	0.41	0.31	0.28
HD 154368	0.35	0.39	0.26
HD 161056	0.31	0.41	0.29
HD 169454	0.37	0.34	0.29
HD 170740	0.31	0.40	0.29
HD 205367	0.41	0.32	0.27

3. Model line profiles

In order to use the fact that both $^{12}CH^+$ and $^{13}CH^+$ lines have the same opacity profile $\tau(v)$, we must fit the $^{12}CH^+$ absorption with a parametrised model and scale it to $^{13}CH^+$.

We considered using Voigt profiles to account for the intrinsic line profiles of the CH^+ vibronic lines. In order to fit the low-level broad wings (e.g. Stahl et al. 1989) towards ζ Oph with an hypothetical Lorentzian core, Einstein A values of order 10^9 s^{-1} are required. Gredel. et al. (1993) quote an oscillator strength of $f_\circ = 0.00545$, or $A = 2.258 \times 10^{-4}$, for $^{12}CH^+ \lambda 4232\, \Pi{-}\Sigma(0,0)$ and $f_\circ = 0.00331$, or $A = 1.568{\times}10^{-4}$, for $^{12}CH^+ \lambda 3957\, \Pi{-}\Sigma(1,0)$. We therefore used simple Gaussian profiles to describe the lines.

We preferred to fit the two overtones separately, and thus obtain independent measurements with which to assess the role of systematics. A simultaneous fit of both overtones could have helped constrain the opacity profiles, which in our separate fits do not always share the same Gaussian components.

The fitting algorithm is as follows.

1. Extract a 1.5 Å spectrum $F(\lambda)$ centred on the CH^+ line, $\lambda_1 < \lambda < \lambda_2$.
2. Define a baseline $F_c(\lambda)$ with a 4−17th order Legendre polynomial to the data, as in Sembach & Savage (1992), $F_c(\lambda) = \sum_{i=1}^{l} a_i P_i[(\lambda - \lambda_1)/(\lambda_2 - \lambda_1)]$.
3. Fit for the $\{a_i\}_{i=1}^{l}$ coefficients in a least square sense, ignoring the neighbourhood of the ISM and telluric lines, and weighting the data to improve the quality of the baselines near the interstellar absorption lines. Store the rms dispersion of the residuals as the spectrum's noise, σ_F. σ_F is updated after fitting the parametrised model; it is replaced by the dispersion of the residuals in Step 8.
4. Define a model spectrum with
$$F^\star_m(\lambda) = F_c(\lambda) \exp(-\tau(\lambda)), \quad (4)$$
where the line absorption opacity τ is a superposition of $n_g = 1$ to 6 Gaussians on each isotope, with $^{13}CH^+$ components sharing the parameters of the $^{12}CH^+$ components, except their centroids are translated by a fixed velocity shift Δv_{iso}, and their amplitude are scaled by a factor $f = {}^{13}CH^+/{}^{12}CH^+$, which is a free parameter in our fit:
$$\tau(\lambda) = \sum_{i=1}^{n_g} \left[\tau_i^\circ \exp\left(-0.5(\lambda - \lambda_i^\circ)^2/\sigma^{\circ 2}_i\right) + f\, \tau_i^\circ \exp\left(-0.5(\lambda - \lambda_i^\circ(1 + \Delta v_{iso}/c))^2/\sigma^{\circ 2}_i\right)\right]. \quad (5)$$
The value of Δv_{iso} depends on the overtone and is adjusted iteratively on ζOph and checked for consistency on all targets. We use $\Delta v_{iso}(3957) = 32.721$ km s^{-1}, $\Delta v_{iso}(4232) = -18.967$ km s^{-1}, with uncertainties of ∼0.4 km s^{-1} (roughly 1/10 the resolution element).
5. Convolve the model spectrum with the instrument response, B_λ:
$$F_m(\lambda) = \int d\lambda' F^\star_m(\lambda') B(\lambda - \lambda'). \quad (6)$$
We estimate the instrumental response from the arc lamp spectrum. The smallest line-widths are indicative of resolving powers of ≈83 000 ± 2000 rather than the nominal 75 000 for our setup. The instrumental response is approximated to a Gaussian, with a FWHM given by $\lambda_\circ/83\,000$, where $\lambda_\circ$ is the center wavelength of each CH^+ overtone.
6. Calculate the goodness of fit function
$$\chi^2 = \sum_j (F(\lambda_j) - F_m(\lambda_j))^2/\sigma_F^2, \quad (7)$$
using the noise from Step 3. We use a single noise value and neglect possible variations of the noise level, as would be the case for Poisson statistics. The noise variations are important for very steep spectra, which is not our case, or under deep absorption lines. But the accuracy of the model line profiles under $^{12}CH^+$ is generally not important to infer isotope ratios (only the wings matter).
7. Optimize the model parameters by minimizing χ^2. Perform an initial estimate of the global minimum with a genetic algorithm (`pikaia`, Charbonneau 1995), and optimize with the downhill simplex method (`amoeba`, Press et al. 1986).
8. Update the noise of the stellar spectrum by replacing σ_F with the rms dispersion of the residuals (the difference between the observed and model spectra).
9. Estimate the uncertainty in model parameters by two methods:
   (a) search parameter space one parameter at a time to find the region enclosing 68.3% confidence for the χ^2 distribution with one degree of freedom, thus obtaining different upwards and downwards error bars and accounting for statistical bias,
   (b) estimate 1σ uncertainties from the curvature matrix of χ^2 (i.e. approximate to normal errors).

The UVES spectra are oversampled, so that the spectral datapoints are correlated. Independent datapoints are separated by roughly one resolution element, of $\Delta\lambda = \lambda/75000 \approx 0.05$ Å. Since the spectra are sampled with an interval of 0.01 Å, $N_{cor} \sim 5$ consecutive datapoints are correlated. In some cases the number of Gaussian components involves as many free-parameters as independent data points (as for HD 154368 and HD 169454). Some Gaussian components may thus be redundant. But we caution that our purpose is to obtain isotopic ratios, not to report on the velocity structure of the ISM in CH^+. To constrain the opacity profile consistently we would have had to fit the two overtones simultaneously.

The correlation between the spectral datapoints is ignored when fitting for the parametrised model. The off-diagonal

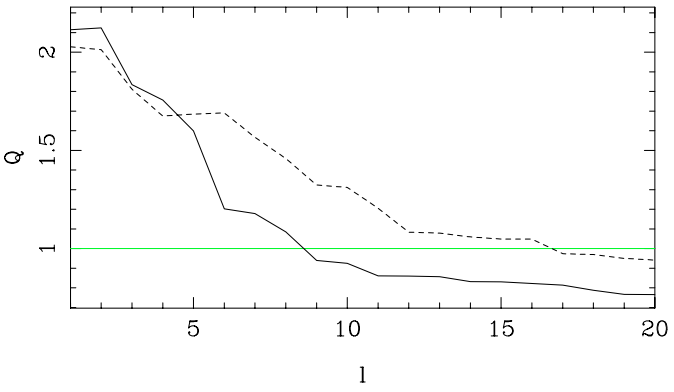

Fig. 2. The ratio of measured to expected noise, Q, as a function of the order of the Legendre polynomial used to define the baselines, l. The data are for 25 exposures of HD 170740 on June 15th, for two 1.5 Å spectral regions centred on λ4232 (solid line), and on λ3957 (dotted line).

terms of the covariance matrix add terms to the χ^2 goodness-of-fit estimator (Eq. (7)). The number of additional terms is roughly $N_{\rm cor}$ per diagonal element, which increase χ^2 by a factor $N_{\rm cor}$. But the noise estimate from the dispersion of the residuals also increases due to the correlation of the datapoints, the actual noise should be $\sigma_F \times \sqrt{N_{\rm cor}}$. Both corrections cancel out and leave χ^2 as in Eq. (7).

We tested for systematic noise by comparing the noise in the nightly coadded spectra, $\sigma_{\rm coadd}$, with that expected from the noise in each of the $N_{\rm exp}$ individual exposures, σ_1. For thermal noise it should hold that $\sigma_{\rm coadd} = \sigma_1/\sqrt{N_{\rm exp}}$. We define $Q = \sigma_1/(\sqrt{N_{\rm exp}}\sigma_{\rm coadd})$, and raise the order of the baselines until $Q \sim 1$. The tests were run for the case of HD 170740, which presents the most ragged continuum. The reference baseline is defined on the coadded spectrum, and the noise is given by the dispersion of the residuals, excluding the spectral regions affected by the ISM lines (these regions are defined in Fig. 12). We scale the reference baseline to the line-free continua of single exposures using the ratio of their median values. Figure 2 shows we need to reach orders of $l \sim 15$ for λ3957, and of $l \sim 8$ for λ4232. Below these orders the continua are affected by systematic noise. Unfortunately the level of systematic noise changes for each observation and setting, so that we can only use the tests on HD 170740 as guidelines for the other lines of sight. In practice we chose the smallest order that is compatible with the data, without exceeding the limits in HD 170740.

The isotopic ratio derived from the fits is the ratio of the column densities of each isotope, $R = N(^{12}CH^+)/N(^{13}CH^+)$. With the best fit f we can calculate $R = 1/f$ for a line of sight with constant R. We neglect the small difference in oscillator strength between $^{12}CH^+$ and $^{13}CH^+$. The two ions have slightly different vibrational structures which will lead to small changes in the $f_\circ$ values for individual vibrationally resolved transitions (J. Tennyson, private communication). We are thus neglecting $f_\circ$-value differences of the order of the relative difference in reduced mass, or $\Delta f_\circ/f_\circ \sim 1/170$.

In taking statistics on the values of $R = 1/f$ in the local ISM care must be taken to assess the significance of measurements along individual sightlines. The uncertainties on individual fits do not include the systematic error involved in baseline definition. If baselines were known a priori, the expectation value and uncertainty on f for each individual sightline would be obtained from the statistics of multiple measurements of the same quantity. Thus, in the absence of this systematic error, $\langle f\rangle$ and $\sigma(f)$ correspond to the weighted average and quadratic sum of the weighted uncertainties, where the weights are taken as the inverse variance of each measurement, $1/\sigma^2$:

$$\langle f\rangle = \sum_{i=1}^{N} f_i w_i, \tag{8}$$

$$\sigma_1^2(f) = \sum_{i=1}^{N} (\sigma_i\, w_i)^2 = 1/\sum_{i=1}^{N} (1/\sigma_i)^2, \tag{9}$$

for N measurements on a given sightline, and where the individual errors are those derived from the curvature matrix.

To estimate the systematic error involved in baseline definition, we compare a posteriori the scatter of individual measurements with that expected from the noise level. We use the rms dispersion

$$\sigma_2(f) = \sqrt{\sum_i w_i\ [(f_i - \langle f\rangle)]^2}. \tag{10}$$

The uncertainty $\sigma_1(f)$ neglects the systematic errors. $\sigma_2(f)$ uncertainties will give larger error bars, but are probably too conservative considering we are in fact repeatedly measuring the same quantity. Thus the actual uncertainty on our measurement of f for each sightline is intermediate between $\sigma_1(f)$ and $\sigma_2(f)$. For this reason we list both values. We have setv $\sigma_2 = \sigma_1$ if $\sigma_2 < \sigma_1$, as is the case when only one ratio is available to sample the effects of systematic uncertainties in the continuum definition (or when one ratio has much higher weight than the others).

4. Results

An application of the fitting procedure described in Sect. 3 to our sample of 10 lines of sight gives the best fit parameters and isotopic ratios listed in Table 3. We show a selection of some of our results in Figs. 3–12. Full details can be found in complete versions of Figs. 3–12 in the electronic version of this paper, which includes nightly spectra and the complete dataset.

The isotopic ratio $f = {}^{13}C/{}^{12}C$ is better suited as free parameter than $R = 1/f$ for the purpose of fitting individual spectra, and subsequently averaging the best fit values. For noisy data the error propagation when using R would involve second order expansions in $R(f)$ when calculating averages and dispersions. In what follows we prefer to list our results in terms of f, and revert to the more common usage of R in Sect. 5 when comparing with previous data.

Table 3 lists the isotope ratios and best fit parameters. It is apparent the λ4232 line generally gives the best estimate of R. We note from Table 3 that the normal errors are good approximations to the 68.3% confidence limits, which justifies their subsequent use in the weighted averages. We also note the weighted average of several measurements for the same line of

Table 3. We list $f \times 10\,000$ to improve the clarity of the table. $\sigma(f)$ refers to the Gaussian errors (those derived from the χ^2 curvature matrix). The average values are quoted as $\langle f \rangle \pm \sigma_1(\sigma_2)$ (see text for details), and exclude the coadded spectra. Equivalent widths for $^{12}CH^+$, W_λ, are given in mÅ. The stars select the measurements included in the combined values of R; the selection are discussed in the text.

	λ3957				λ4232			
target, date	f	$\sigma(f)$	n_g	W_λ	f	$\sigma(f)$	n_g	W_λ
ζOph, June 14	$\star\ 138^{+8.9}_{-12.1}$	10.4	3	13.72(3)	$\star\ 121^{+9.8}_{-8.7}$	9.18	3	23.40(5)
ζOph, June 15	$\star\ 128^{+14.8}_{-12.3}$	13.5	3	13.68(4)	$\star\ 126^{+8.8}_{-8.5}$	8.67	3	23.37(5)
ζOph, June 16	$\star\ 132^{+13.6}_{-13.8}$	13.7	3	13.73(4)	$\star\ 124^{+12.4}_{-9.5}$	10.8	3	23.45(6)
ζOph, coadd	$111^{+4.4}_{-9.7}$	6.51	3	13.74(2)	$124^{+4.5}_{-5.2}$	4.82	3	23.42(3)
Average	133.67 ±7.06(7.06)				123.73±5.44(5.44)			
	$\langle f \rangle$ = 127.44±4.31(5.73)				$\langle R \rangle$ = 78.47±2.65(3.53)			
HD110432, June 14	$85.6^{+17.8}_{-15.0}$	16.3	2	7.85(3)	$\star\ 162^{+17.3}_{-10.3}$	13.2	2	13.82(4)
HD110432, June 15	$134^{+18.0}_{-12.7}$	15.1	2	7.65(2)	$\star\ 146^{+15.8}_{-10.5}$	12.9	2	13.83(5)
HD110432, June 16	$66.8^{+16.9}_{-13.3}$	14.9	2	7.71(2)	$\star\ 181^{+22.6}_{-10.7}$	15.6	2	13.86(5)
HD110432, coadd	$86.4^{+13.9}_{-9.9}$	11.7	2	7.71(2)	$159^{+16.4}_{-11.3}$	13.6	2	13.64(4)
Average	$\langle f \rangle$ = 160.86±7.94(13.76)				$\langle R \rangle$ = 62.17±3.07(5.32)			
HD152235, June 14	$\star\ 115^{+7.0}_{-9.9}$	8.32	3	24.81(5)	$\star\ 116^{+8.0}_{-6.7}$	7.32	3	41.14(8)
HD152235, June 15	$96^{+11.0}_{-14.1}$	12.4	3	25.03(7)	$\star\ 108^{+7.8}_{-7.0}$	7.38	3	40.99(8)
HD152235, June 16	$135^{+9.2}_{-10.5}$	9.79	3	24.85(5)	$\star\ 113^{+8.6}_{-7.1}$	7.84	3	41.16(8)
HD152235, coadd	$106^{+7.3}_{-6.8}$	7.08	3	24.82(4)	$114^{+6.6}_{-4.4}$	5.39	3	41.06(6)
Average	112.33±4.33(4.33)							
	$\langle f \rangle$ = 112.90±3.84(3.84)				$\langle R \rangle$ = 88.58±3.01(3.01)			
HD152236, June 15	$\star\ 62.1^{+32.1}_{-35.2}$	33.6	5	9.67(5)	$17.4^{+34.6}_{-34.6}$	34.6	5	18.01(9)
					$\langle R \rangle$ = > 61.39			
HD152424, June 14	$\star\ 233^{+17.0}_{-16.4}$	16.7	6	20.39(6)	$\star\ 132^{+17.8}_{-17.8}$	17.8	6	36.43(11)
	$\langle f \rangle$ = 185.72±12.18(50.40)				$\langle R \rangle$ = 53.85±3.53(14.61)			
HD154368, coadd	$\star\ 184^{+14.0}_{-12.8}$	13.4	6	10.64(3)	$\star\ 136^{+22.2}_{-22.2}$	22.2	6	19.03(9)
	$\langle f \rangle$ = 171.18±11.47(21.24)				$\langle R \rangle$ = 58.42±3.91(7.25)			
HD157038, June 14	$\star\ 157^{+15.0}_{-16.2}$	15.6	4	28.21(8)	$63.4^{+22.1}_{-22.1}$	22.1	4	48.81(19)
					$\langle R \rangle$ = 63.69±6.33			
HD161056, June 14	$\star\ 85.7^{+26.3}_{-26.3}$	26.2	3	11.62(4)	$182^{+16.3}_{-16.3}$	16.3	3	20.51(7)
HD161056, June 15	$\star\ 56.4^{+16.8}_{-18.7}$	17.6	3	11.28(4)	$196^{+28.7}_{-28.7}$	28.7	3	20.26(11)
HD161056, June 16	$\star\ 75.5^{+20.2}_{-20.2}$	20.2	3	10.94(4)	$281^{+36.2}_{-36.2}$	36.2	3	20.07(14)
HD161056, coadd	$79.9^{+13.3}_{-13.5}$	13.3	3	11.23(3)	$220^{+27.7}_{-27.7}$	27.7	3	20.26(11)
Average	$\langle f \rangle$ = 68.94±11.84(11.97)				$\langle R \rangle$ = 145.05±24.91(25.18)			
HD169454, June 14	$51.6^{+50.8}_{-49.4}$	49.9	6	10.70(11)				
HD169454, June 15	$\star\ 141^{+20.6}_{-25.4}$	22.8	6	10.23(5)				
HD169454, June 16	$\star\ 123^{+31.4}_{-26.6}$	29	6	10.27(6)				
HD169454, coadd	$112^{+24.2}_{-24.2}$	24.3	6	10.17(5)	$-125^{+79.0}_{-78.9}$	78.9	6	17.59(28)
Average	$\langle f \rangle$ = 134.12±17.92(17.92)				$\langle R \rangle$ = 74.56±9.96(9.96)			
HD170740, June 14	$50.8^{+32.9}_{-33.8}$	33.3	2	7.98(5)	$\star\ 97.2^{+23.9}_{-19.0}$	21.4	2	13.97(7)
HD170740, June 15	$126^{+34.1}_{-27.2}$	30.5	2	7.98(5)	$\star\ 110^{+21.1}_{-16.2}$	18.5	2	13.91(6)
HD170740, June 16	$77.2^{+38.7}_{-34.8}$	36.7	2	7.82(6)	$\star\ 94^{+21.6}_{-16.8}$	18.9	2	14.07(5)
HD170740, coadd	$\star\ 103^{+28.0}_{-23.8}$	25.9	2	7.85(4)	$91.5^{+21.8}_{-13.9}$	17.4	2	13.97(6)
Average	100.80±11.25(11.25)							
	$\langle f \rangle$ = 101.15±10.32(10.32)				$\langle R \rangle$ = 98.87±10.08(10.08)			

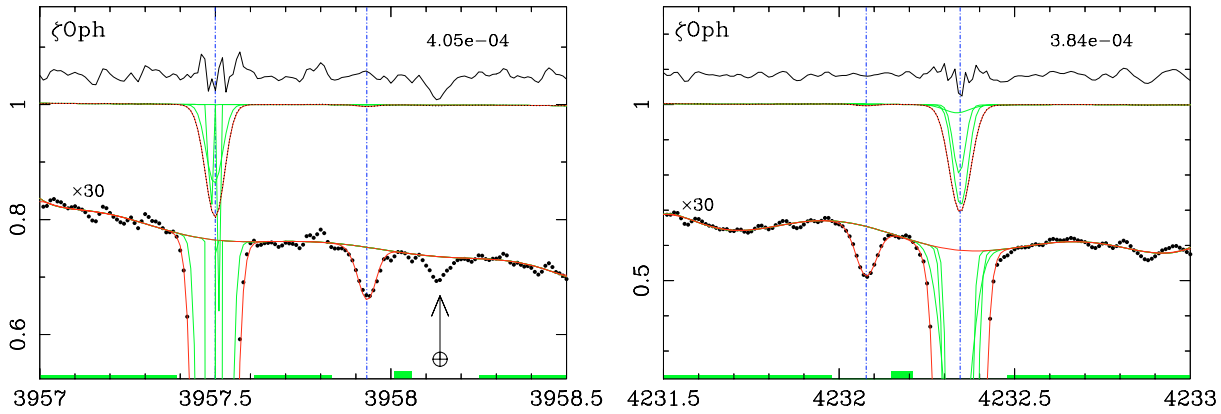

Fig. 3. ζOph spectra. Wavelengths are in Angstroms, and flux densities in arbitrary units. The individual Gaussian components comprising the fit, prior to folding with the instrumental response, are shown only on $^{12}CH^+$ as light gray lines, but are omitted from $^{13}CH^+$ for clarity (see text for details). The vertical dashed lines mark the line centroids, at the average of the Gaussian centroids weighted by their equivalent widths. The units of the y-axis are arbitrary, and are scaled so that the median of the object spectrum is unity. Also shown is a magnified version of the object spectrum, by the factor indicated on the figure, and offset for clarity. The residual spectrum is shown on top of the object spectrum, and is also magnified by the factor indicated on figure. The noise used to compute the significance of the fits is labelled on the top right. The noise is the rms dispersion of the residual spectrum, and is in the same units as the y-axis. The height of the shaded rectangles on top of the x-axis indicates the relative weights used in the baseline definition.

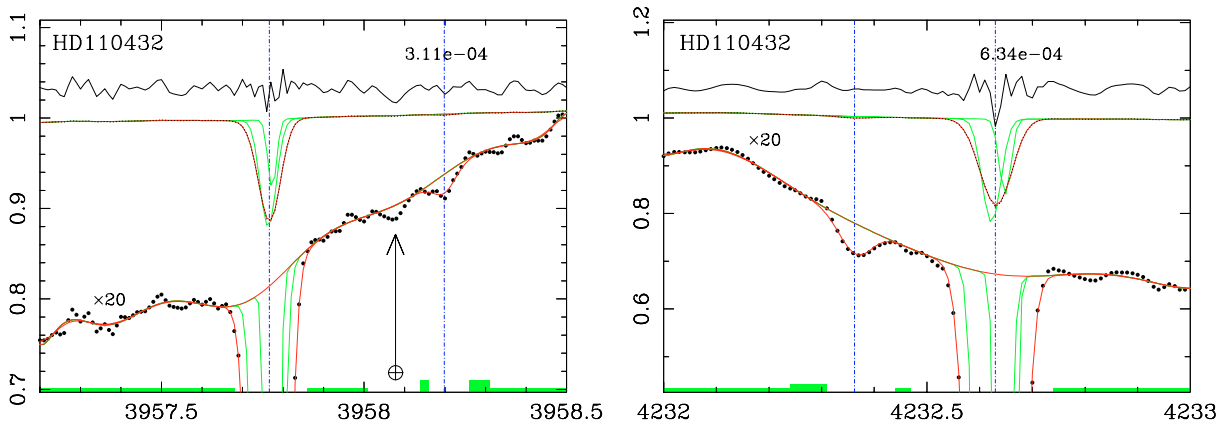

Fig. 4. Same as Fig. 3. The fits on the λ3957 lines are excluded from the combined measurement of R.

sight are consistent, within the errors, with the fit to the coadded spectra (which are in general excluded from the averages), giving confidence in our procedure.

4.1. Notes on individual objects

4.1.1. ζ Oph

From *Hipparcos* results, the distance to ζOph gives an upper limit to the absorbing cloud of 140±14 pc. The spectra of ζOph around the CH^+ lines are shown in Fig. 3, where we have also plotted the Gaussian components on the $^{12}CH^+$ line (the individual components on the $^{13}CH^+$ line are left out for clarity).

Residual features under the absorption lines vary on scales of ∼0.02 Å. These reflect the imperfection in the model line profiles, more Gaussian components reduce these residuals.

The ζOph spectra were acquired at airmasses of 1.8 and 1.7 on the 15th and 16th of June. Both spectra show absorption at 3958.15 Å (at 3958.5 Å in the observatory's rest frame). This is absent in the spectrum from 14th of June and in all other targets. Since all other spectra were acquired with low airmass values compared with that of ζOph on the 15th and 16th, we conclude the 3958.15 Å feature is telluric. We did not attempt to include the 3958.15 Å feature in the fits. The telluric absorption propagates into the residuals, and contributes to the noise level. Note that the telluric feature has no effect on where we set the baseline level, because we assigned zero weights to the spectral points in its neighbourhood.

Stahl et al. (1989) reported $R = 77 \pm 3$[1] from λ4232, using a single Gaussian fit. But Stahl & Wilson (1992) used two Gaussian components to account for the broad wings detected by Crane et al. (1991), and thus obtained a tighter fit to the ζOph CH^+ absorption, with $R = 71\pm3$ for λ4232 and $R = 68\pm7$ for λ3957.

We also find that using two instead of one Gaussian components significantly improves the fit, bringing reduced χ^2 values for the coadded ζOph λ4232 spectrum from 2.07 for one Gaussian (using the noise reference of the two Gaussian fit),

[1] Note their uncertainty is estimated as for σ_1 in this work, in the case where all samples are assigned the same weight.

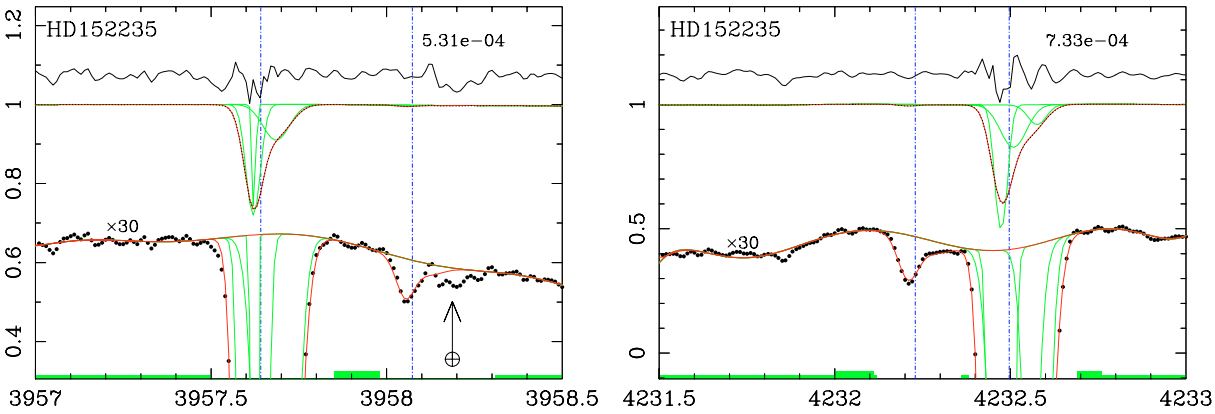

Fig. 5. Same as Fig. 3. The fits on λ3957 for June 15th and 16th are excluded from the combined measurement of R.

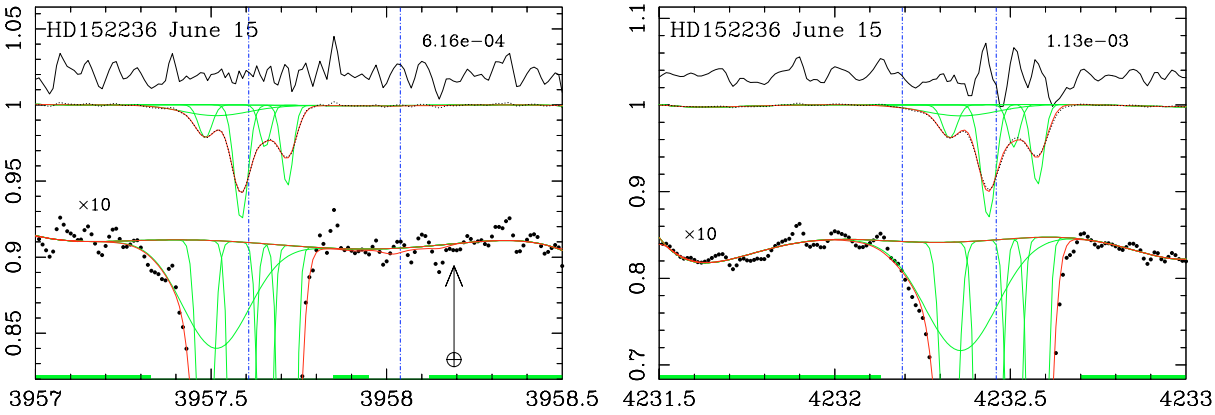

Fig. 6. Same as Fig. 8. No excess absorption is detected on the blue edge of λ4232 $^{12}CH^+$.

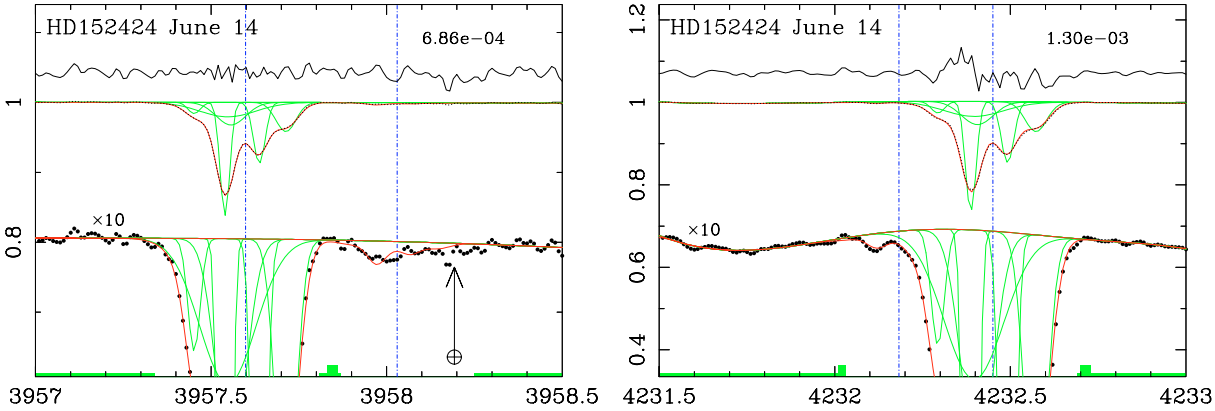

Fig. 7. Same as Fig. 8. $^{13}CH^+$ is visible as excess absorption on the blue edge of λ4232 $^{12}CH^+$.

to 1.05 for two Gaussians. But the resulting average for R is unchanged, we obtain $\langle R\rangle = 78.22 \pm 2.63(3.75)$ with one Gaussian, $\langle R\rangle = 80.20 \pm 2.75(4.19)$ with two Gaussians.

What is the effect of including more than two Gaussians? It is difficult to separate an error in the definition of the continuum baseline from a real increase in confidence level of the fit. We experimented on ζOph with 3 and 4 Gaussians, keeping the noise fixed to the rms dispersion of the residuals in the 2 Gaussian fit. The reduced χ^2 were respectively 0.92 and 0.88 for the 3 and 4 Gaussian fits to the spectral region centred on λ4232 in the coadded spectrum of ζOph. But some of the 4-Gaussians fits to the ζ Oph spectra contained very narrow features, corresponding to unphysical opacity components. Since we cannot separate the uncertainty in the baseline definition, we adopt the smallest number of Gaussians consistent with the dataset (with reduced χ^2 close to 1). We chose 3 Gaussians rather than 2 because Crawford et al. (1994) report a 3-Gaussians decomposition of the ultra-high resolution CH^+ profile toward ζOph. The final value from the UVES data is thus $\langle R\rangle = 78.47 \pm 2.65(3.53)$, with a 3-Gaussian fit.

All R values for ζOph are consistent within 2σ. The value we obtain here is higher than previously reported by

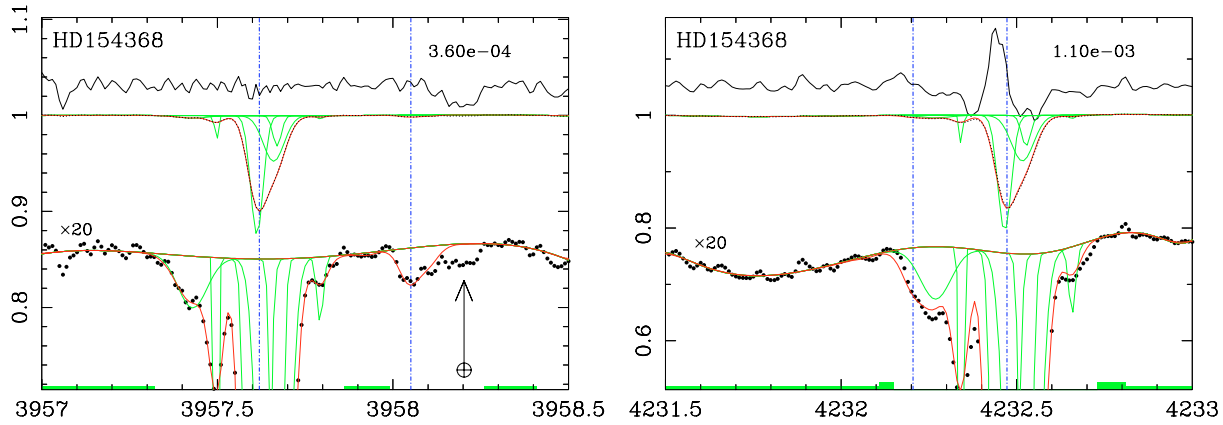

Fig. 8. Same as Fig. 3. This line of sight has blended $^{12}CH^+$ and $^{13}CH^+$ absorption at λ4232. We extrapolate the $^{12}CH^+$ profile at λ3957 (see text for details). $^{13}CH^+$ is visible as excess absorption on the blue edge of $^{12}CH^+$.

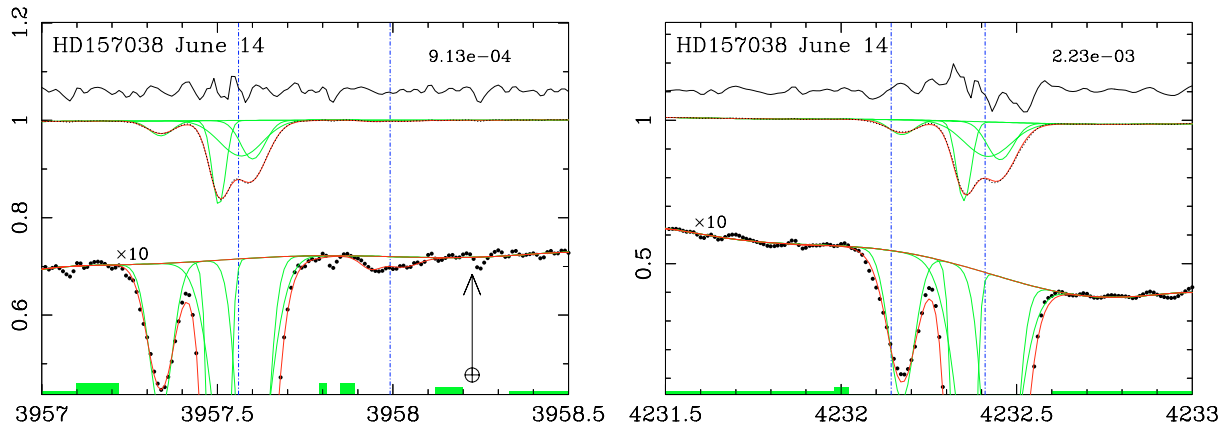

Fig. 9. Same as Fig. 8. The fit for $^{13}CH^+$ absorption on the blue edge of λ4232 $^{12}CH^+$ gives a 3σ detection, but is barely visible in the figure.

Stahl et al. (1992) by 1.6σ, adding the statistical errors in quadrature. For comparison Hawkins et al. (1993) give R = 63 ± 8 for λ4232, 67 ± 19 for λ3957, Crane et al. (1991) give R = 67.6 ± 4.5 for λ4232, and Vanden Bout & Snell (1980) report $R = 77^{+17}_{-12}$, also for λ4232.

The value reported in this article has an accuracy close to that of Stahl et al. (1992), of 71 ± 3. Combining both measurement with identical weights gives our best value for ζOph as R = 74.7 ± 2.3.

In what follows we will nonetheless use the UVES value of R for ζOph to compare with the other lines of sight, $\langle R \rangle$ = 78.47 ± 2.65(3.53) thus relying exclusively on measurements obtained with the same instrument.

4.1.2. HD 110432

The profile from Crawford (1995) is well fit by 1 Gaussian only, but we obtain best results with 2 Gaussians.

The *Hipparcos* distance to HD 110432 is 300 ± 51 pc, which confirms that the CH^+ absorption most likely arises in the Coalsack, at a maximum distance of 180 pc (Franco 1989).

The fit on the λ3957 line is excluded from the combined measurement of R because the adjacent telluric absorption feature could affect the wings of the CH^+ absorption. Also the baseline around λ3957 seems to be strongly affected by systematic noise. The λ3957 values differ from λ4232, which otherwise give consistent numbers for each night.

4.1.3. HD 152235

HD 152235 is a member of the Sco OB1 association, but as discussed by Crawford (1995) the absorbing CH^+ lies in the Lupus molecular cloud, at 170 pc (Murphy et al. 1986).

The profile from Crawford (1995) is fit by 3 Gaussians. Our data, presented in Fig. 5, also required 3 Gaussians for λ3957.

The CH^+ absorption has a red tail than difficults separating both isotopes at 4232 Å, while the telluric absorption feature borders the $^{13}CH^+$ line. It is difficult to pin down the underlying continuum at 4232 Å. We tried two approaches to define the continuum from edge to edge of the CH^+ absorption (from 4232 Å to 4232.7 Å): a free fit (i.e. roughly a straight-line, with zero weights over 4232 Å – 4232.7 Å), and the inclusion of a small non-zero weight mid-way between the two isotopes (see Fig. 5).

The spectrum from 2003 June 14th is clear of telluric absorption (it was observed with the smallest air mass, see Table 1), so both overtones should give consistent values for R. This is why we chose the baseline shown in Fig. 5. The two overtones give consistently high value for June 14th, and also on average. So we are rather confident of the ratio we report.

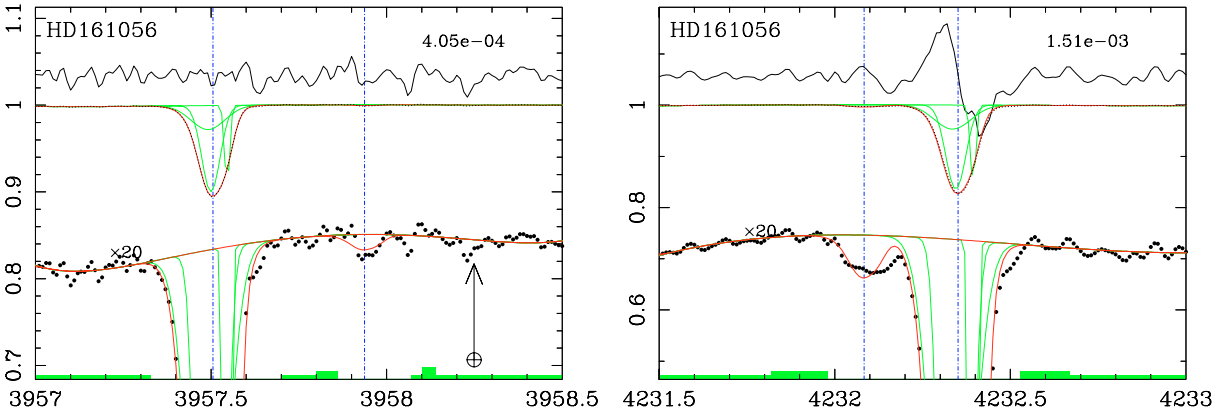

Fig. 10. Same as Fig. 3. None of the λ4232 spectra were used to combine individual measurements of R. There is excess absorption bridging the two isotopes at λ4232. The origin of the additional absorption, whether a telluric or a stellar feature, is unclear.

The fits on λ3957 for June 15th and 16th are excluded from the combined measurement of R because they are affected by telluric absorption under the red tail of $^{13}CH^+$.

Vladilo et al. (1993) reported $R = 126 \pm 29$. Our measurement, which has better accuracy, gives lower value, although still higher than the ISM average (see Sect. 5).

This line of sight gives a significantly higher R value than in HD 110432 at 4.2σ, using the conservative uncertainties σ_2, from the scatter of each individual measurement of R.

4.1.4. HD 152236

Figure 6 presents the CH^+ spectra for HD 152236, along with our fits. Crawford (1995) used 4 Gaussians, but we needed 6.

HD 152236, as HD 152235, is a member of the Sco OB1 association, so that the absorption probably occurs in the Lupus cloud.

There is no manifest absorption at λ3957, but we give the result of the formal fit, which allows assigning a lower limit R value. We take $f_{\rm uplimit} = \langle f \rangle + 3\sigma_1(f)$, and $R > 1/f_{\rm uplimit}$, giving $R > 61.4$ at the 3σ level.

Although the λ4232 line has better signal to noise, both isotopes are blended. We tried to apply the technique described below in the case of HD 154368 (Sect. 4.1.6), but did not obtain significant excess absorption in the blue wing of the main line. The lower limit refers only to the λ3957 measurement.

4.1.5. HD 152424

HD 152424, as HD 152235, is a member of the Sco OB1 association, so that the absorption probably occurs in the Lupus cloud.

Vladilo et al. 1993 report $R = 98 \pm 19$, but this target gives us our lowest R value, of $55.65 \pm 3.55(15.61)$.

The two isotopes are blended at λ4232, so we apply the same technique as for HD 154368 (Sect. 4.1.6). The residuals under the ^{13}CH+ absorption are consistent with the noise, which gives us confidence in the inferred R value. HD 152424 provides our best measurement of R for blended lines, as obtained by keeping the opacity profile fixed to the best fit on λ3957. But defining consistent baselines between the two

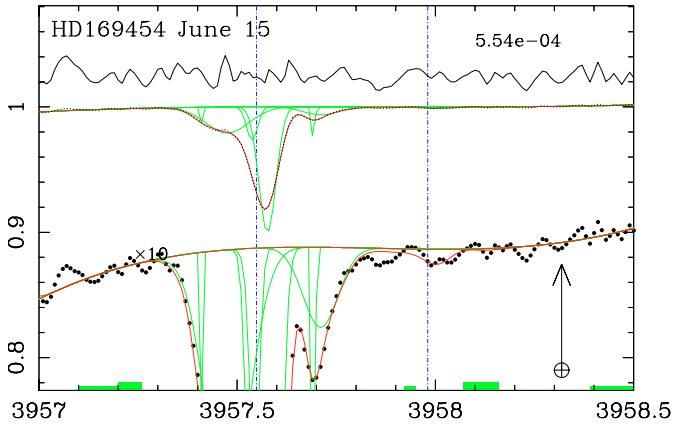

Fig. 11. Same as Fig. 8. The information from λ4232 is not used because f is spuriously negative, and neither is that from λ3957 on June 14th because of a non-ISM absorption feature at 3957.3 Å.

overtones is very difficult without including the baseline as free parameter. So we decided to ignore the significant residuals under the main isotope at λ4232. We include the noisy residuals in the noise estimate, so that the significance of the R values derived from the blended line is lowered.

The importance of quantifying systematic uncertainties is manifest in HD 152424: a visual inspection of Fig. 7 shows the fit under λ3957 is very good, and that the baseline seems smooth. However appeareances can be deceiving: the extrapolation of the λ3957 fit to λ4232 gives a very different value of R. Had we considered only the σ_1 uncertainties, the value for HD 152424 would have been one of the most accurate. But because CH^+ towards HD 152424 is so broad the conservative uncertainty σ_2 is much higher than σ_1 and reflects the systematic uncertainty involved in the baseline definition.

4.1.6. HD 154368

This target was selected from the survey of Gredel et al. (1993).

The CH^+ absoprtion for HD 154368 (with an *Hipparcos* distance of 364.8 ± 128.3 pc) shown in Fig. 8 has four conspicuously distinct velocity components. The two isotopes are manifestly blended for the λ4232 transition.

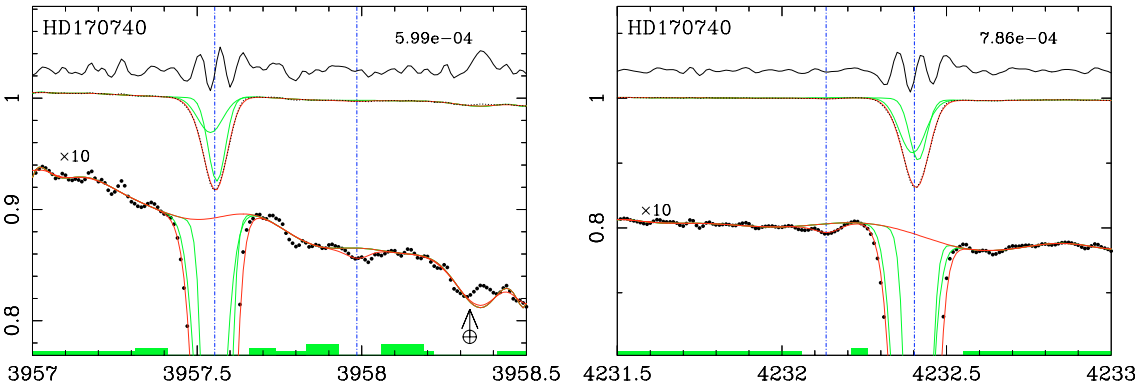

Fig. 12. Same as Fig. 8. The spectra around λ3957 have ragged baselines, presumably due to instrumental fringing. Only the coadded spectrum at λ3957 is used for subsequent averaging of R with that from λ4232.

Our data cover the two overtones in the same UVES dichroic setting simultaneously, and the spectral resolution is expected to be constant with wavelength in such an instrumental setup. After checking we had no detectable trend of varying resolution by measuring the arc line widths, we attempted fitting λ4232 using the results of the λ3957 fits.

A fit of both overtones simultaneously would be counterproductive because the λ4232 region has better sensitivity, and would dominate the fit, placing Gaussian components of $^{12}CH^+$ under the rarer isotope. Instead we kept the $^{12}CH^+$ opacity profile as a function of velocity $\tau(v)$ as inferred from the λ3957 fit. We then scaled $\tau(v)$ to $\tau(\lambda)$ for the λ4232 region, which implies scaling component widths and separations in wavelengths. After setting baselines as in the unblended case, the optimization involved two free parameters, the scaling factors on the $^{12}CH^+$ and $^{13}CH^+$ opacity profiles.

The fits shown in Fig. 8 are rather poor in the case of λ4232. Uncertainties in the baseline determination resulted in significant residuals under the main isotope line. But these do not affect the $^{13}CH^+$ absorption. We recompute the noise level from the residuals, including the baseline uncertainties. The uncertainties on R tabulated in Table 3 are a result of this exaggerated noise level.

4.1.7. HD 157038

This line of sight also has blended absorption at λ4232, and we apply the same technique as for HD 154368. But the results on λ4232 are useless because they are too sensitive on the baseline definition, so we avoided the use of λ4232 altogether.

Hawkins & Meyer (1989, and references therein) give $R = 38\pm12$ from λ4232 and use a distance of 1.7 kpc to HD 157038. We confirm this line of sight is enriched in ^{13}C, with a lower R value than the average ISM value (see Sect. 5.1).

4.1.8. HD 161056

$^{13}CH^+$ absorption towards HD 161056 (selected from Gredel et al. 1993) is very weak at λ3957, and yet conspicuous at λ4232 (see Fig. 10). We first attempted to fit the two overtones separately, and found widely discrepant values: $f(3957) = 68.9 \pm 11.8(12.0)$, and $f(4232) = 159.3 \pm 5.6(19.1)$. The two isotopes may be blended at λ4232. We thus applied the same technique as for HD 154368, extrapolating the λ3957 opacity profile to λ4232. But the inferred isotope ratios were still very different (see Table 3). There must be additional absorption bridging the two overtones at λ4232, not due to CH^+: the red tail of λ4232 is also seen at λ3957, while the absorption at the blue edge of λ4232 is not seen at λ3957. We cannot identify the nature of the additional absorption, so we choose to exclude λ4232 from the combined measurement of R in HD 161056.

The *Hipparcos* distance to HD 161056 is 425.7 ± 145.5 pc.

4.1.9. HD 169454

This line of sight, selected from Gredel et al. (1993), exibits at least 4 distinct velocity components. We use 6 Gaussians to describe the profile, but did not attempt to compare reduced χ^2 when varying the number of Gaussians because of the uncertainties in the baseline definition.

The total number of free-parameters used to describe the main line is 6×3, with 3 parameters per Gaussian. The zero-absorption line width for HD 169454 is ~0.8 Å, or 80 spectral datapoints. But the number of independent resolution elements under $^{12}CH^+$ is about 16. Thus 18 free parameters may seem slightly excessive. But over-constraining the opacity profile is of no consequence to the derived isotopic ratio.

We use the same technique as for HD 154368 to model the blended $^{12}CH^+$ and $^{13}CH^+$ absorption at λ4232, but do not obtain satisfactory results. The fits on λ4232 are shown in Fig. 11 for completeness, and are not included in the combined measurement of R towards HD 169454. An unphysical value of f is obtained, but this value is still consistent with zero $^{13}CH^+$ within the uncertainties. Also excluded from the combined measurement of R is the fit to λ3957 from June 14th because it shows non-ISM absorption at 3957.3 Å. The λ3957.3 feature is not seen in other spectra acquired at similar airmass (e.g. that of HD 152235 on June 15th), and is either an instrumental artifact or the effect of passing clouds.

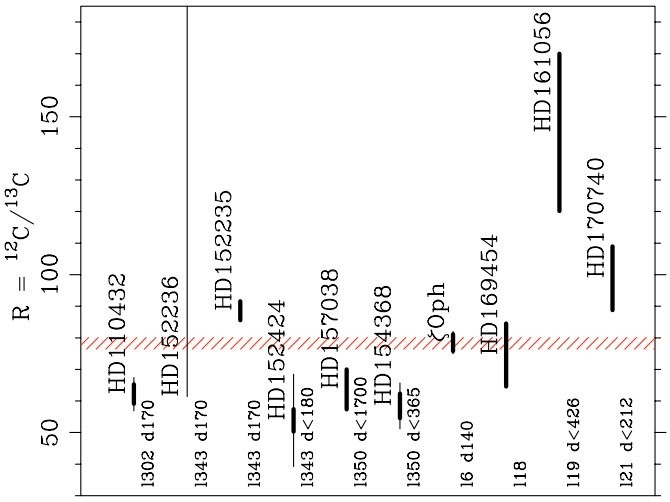

Fig. 13. A plot of individual R values for the lines of sight studied in this work. The thick lines are $\pm\sigma_1$ uncertainties, from the weighted average uncertainty of individual measurements. The thin lines are $\pm\sigma_2$ uncertainties, from the scatter of measurements for a given line of sight, and are set equal to σ_1 if $\sigma_2 < \sigma_1$. The hatched box is the weighted average of the measurements in the figure, and should be representative of the local ISM. This value is 78.27 ± 1.83. The height of the hatched rectangle is $\pm 1\sigma$. Galactic longitude and distance in parsec are indicated to the bottom right of each target.

4.1.10. HD 170740

This line of sight, selected from Gredel et al. (1993), is important since it has the highest R value among those considered in this work, together with HD 161056. The Hipparcos distance to HD 170740 is 211.9 ± 42.4 pc.

Unfortunately instrumental fringing, especially at λ3957, limits the accuracy of the fits. The λ3957 $^{13}CH^+$ line is only marginally detected in individual nights, but we give the formal fits. The value we report relies on the nigthly spectra for λ4232, and on the coadded spectrum for λ3957.

5. Discussion

5.1. Observed scatter and comparison with other sightlines

Figure 13 summarises our results. The isotopic ratio R is lower for HD 110432 than for HD 152235 by 4.3σ, and lower than for HD 170740 by 3.2σ. In this comparison we have used the conservative uncertainties σ_2, derived from the scatter of R for different nights and different overtones.

The weighted average of R for the 9 lines of sight considered in this work with $^{13}CH^+$ detections is $R_{\rm ISM} = {}^{12}C/{}^{13}C = 78.27 \pm 1.83$. The weighted 1σ dispersion of the data is 12.7. The hypothesis that the observed scatter is derived from a single value of R can be tested by calculating the corresponding value of χ^2/ν, where $\nu = 8$ is the number of the degrees of freedom (the number of line of sights less one free parameter). We obtain $\chi^2/\nu = 6.0$, which discards the hypothesis at a confidence level of essentially 1.

The observed scatter is not due to the galactocentric abundance gradient studied by Hawkins & Meyer (1989), and predicted by Galactic chemical evolution models. The targets in our sample all lie within 30 deg of $l = 0$, and at distances of at most ~200 pc (except for the clouds toward HD 157038 and HD 169454, whose distances are unknown). Figure 13 also gives longitude and distance information for each target.

Our value for $R_{\rm ISM}$ is significantly higher than those for the Pleiades, ξPer and P Cyg. Vanden Bout & Snell (1980) measured 49^{+12}_{-8} and 59^{+24}_{-13} for 20 Tau (Maia in the Pleiades) and ξPer. Hawkins & Jura (1987) report R values of 46 ± 15 for ξPer, 40 ± 9 for 20 Tau, 41 ± 9 for 23 Tau (also in the Pleiades), and 45 ± 10 for P Cyg. Hawkins et al. (1993) confirm a low value of 49 ± 15 for ξPer. Even taking 3σ errors, the measurements by Hawkins et al. are below our results. One can ask whether the ^{13}C enrichment in the Pleiades is due to contamination from past stellar winds in the cluster itself.

Aside from the R values obtained by other groups and quoted so far in this work, there are also those from Centurion & Vladilo (1991) for μNor (67 ± 6) and HD 26676 (64 ± 6), which differ at 2σ with our average ISM value (including its scatter).

5.2. Are there D/H variations in the local ISM?

From our data set, the values of R vary by 7σ in the local translucent clouds, where σ is the uncertainty in the weighted average value $\langle R_{\rm ISM} \rangle$. This is strong indication that the ISM at the same galactocentric distance is not completely mixed. If this is the case in the chemical composition of the ISM in general, then one expects that the D/H ratios in the local ISM will also differ from place to place. Moos et al. (2002) (see also Vidal-Madjar 2002) summarise the *FUSE* results towards nearby white dwarfs, located within 100 pc of the Sun. The D I/H I ratios measured with interstellar D I and H I Lyman absorption varies by less than ~10% towards 7 white dwarfs within 100 pc of the Sun, at the limits of the Local Bubble. The fractional standard deviation of D I/H I (the ratio of the scatter in the data to its weighted average) is 12%, but cannot be distinguished from a single D I/H I value within the uncertainties. By contrast, the D I/H I ratios obtained with IMAPS show a factor of 2 scatter towards γ^2 Vel, ζ Pup and δ Ori, beyond the Local Bubble, at distances of 300−500 pc (Jenkins et al. 1999; Sonneborn et al. 2000).

Is the scatter in the observed interstellar D I/H I due to variations in D/H? The primary objective of the IMAPS D I/H I observations, as stated by Sonneborn et al. (2000), is "to determine D/H with sufficient accuracy to test for spatial inhomogeneity". But the D/H ratio is notoriously difficult to measure, and often involves the use of several different instruments. The H I lines are > 100 km s^{-1} broad and saturated so that N(H I) is measured from the Ly α damping wings, while N(D I) is best measured from Ly δ or Ly ϵ in the case of the IMAPS targets. The D/H ratio involves carefully considering the effect of the underlying stellar continua and the contribution from other interstellar H I components in the rising part of the curve of growth (with a high ratio of equivalent width to opacity compared to the main absorption line). Chemical fractionation and selective dissociation of HD affects D I/H I for

lines of sight where H_2 is observed, and differential acceleration by radiation pressure could displace D I relative to H I in the diffuse ISM. Bruston et al. (1981) assign the D I/H I scatter known at the time to such effects, and estimate a value of unperturbed D/H almost a factor of two higher than the observed average D/H of 1.5×10^{-5}.

In addition Draine (2004) argues for variable depletion of D onto dust grains, such that the gas phase D/H would be a function of dust processing, which is in turn a function of Galactic environment. The variations in D I/H I do not seem to be a faithful measure of D/H.

5.3. Inefficient mixing in the local ISM

What is the level of elemental homogeneity in the ISM? What is the power-spectrum of the dispersion in elemental abundance relative to the total metalicity? Does heterogeneity increase with size?

At least one extreme of spatial scale indicates perfect mixing: the meteoritic evidence favours mixing at the molecular level of interstellar dust from different origin, during the formation of the solar system. Zinner et al. (1991, their Table 1) measured $^{1}2C/^{13}C$ values from 3 to 1000 in different SiC grains found in the Murchison meteorite. At some point in the presolar cloud the SiC grains must have been mixed from a previously heterogenous distribution.

In a recent review of interstellar turbulence and mixing, Scalo & Elmegreen (2004) summarise current knowledge of the level of elemental heterogeneity in the ISM. The stellar return to the ISM should be spotty and poorly mixed. Scalo & Elmegreen explain that in contrast with diffusive processes, turbulence transport does not homogenize the gas at the atomic level. Yet the heterogeneity is notoriously difficult to detect. The available gas-phase diagnostics depend on local excitation, while the stellar data give upper limits only on the dispersion of elemental composition.

But the $^{12}CH^+/^{13}CH^+$ ratio, in contrast to D I/H I, is a particularly sensitive probe of the mixing efficiency of the ISM. In terms of the fractional standard deviation used by Moos et al. (2002), the scatter we have measured is $\sigma_{\rm ISM}/\langle R_{\rm ISM}\rangle = 16.2\%$ on a scale of 100 pc. Considering the precise location of the absorbing material is unknown, we take the Moos et al. (2002) measurement of a 10% scatter of D I/H I from the mean value as a indication of inhomogeneity of the local ISM, over 100 pc scales. This value is similar to the variations reported in this work, even though D is burned in stellar interiors, rather than produced as is the case of ^{13}C. Although their absolute yields are different, the mixing process (i.e. passive scalar turbulence, Scalo & Elmegreen 2004) should be similar for both species.

5.4. Is the solar value for R comparable to ISM measurements?

The terrestrial value of R is 90 (Rosman & Taylor 1998), and is usually extrapolated to the Sun. However, the preliminary results of Ayres et al. (2005) indicate a photospheric carbon isotopic ratio of 70. The average value of our measurements of R in the local ISM, 78.27 ± 1.83, is slightly lower than the solar value of 90 (or even higher than the photospheric value of 70). But in fact $\langle R_{\rm ISM}\rangle$ is indistinguishable from the solar carbon isotope ratio given the observed scatter of 12.7.

Models of galactic chemical evolution predict an enhancement of ^{13}C relative to ^{12}C with time. Thus our result that $^{13}C/^{12}C$ has essentially remained constant over the past 4.5 Gyr is surprising. The inconsistency is worsened when comparing with the preliminary results of Ayres et al. (2005). We may be affected by a sampling bias. Around 30 lines of sight or more are required to faithfully estimate $\langle R_{\rm ISM}\rangle$.

But is the solar value truly representative of the ISM at the time of collapse of the solar nebula? The process of CO fractionation followed by condensation on cold dust grains may have increased ^{13}C in the pre-solar dust. With an enhanced dust-to-gas ratio through sedimentation in the accretion disk of the Sun, the result may have been a modification in the final R value.

We imagine a ^{13}C-rich disk with a dust mass of 0.01 $M_\odot$, dust to gas ratio of unity, accreting on a zero-age Sun with metalicity $Z = 0.01$. The ^{13}C-poor atmosphere of the disk may have been blown away by the early solar wind, so that once the accretion of the disk is concluded, the Sun reaches $Z = 0.02$ and higher $^{13}C/^{12}C$ than the pre-solar cloud.

Aside from the possibility of preferential accretion of ^{13}C over ^{12}C, there is evidence that the solar nebula differed in composition from the bulk ISM. For instance the metalicity of B stars in Orion is lower than that of the Sun, even after 4.5 Gyr of Galactic chemical evolution, indicating that the Sun must have been exceptionally metal-rich. This discrepancy has been interpreted in the framework of Galactic diffusion (Wielen 1977), by which the Sun diffused from its birthplace outwards in Galactocentric radius by $\Delta r_{\rm GAL} = 1.9$ kpc. Since $^{13}C/^{12}C$ is also predicted to increase with $r_{\rm GAL}$, Galactic diffusion may bring in agreement the ISM and solar values of R at the time of solar birth (Wielen & Wilson 1997).

But perhaps the most compelling evidence that isotopic ratios in the Sun cannot be taken as direct constraint on the bulk ISM are isotopic anomalies in meteorites, such as the presence of extinct radionuclides. For instance Zinner et al. (1991) found that $^{26}Al/^{27}Al \approx 1$ in the pre-solar nebula. They measured the concentration of the decay product of ^{26}Al, ^{26}Mg, locked in SiC grains from the Murchison meteorite. But in other meteorites $^{26}Al/^{27}Al \approx 1/4000$ in Al-rich minerals from refractory inclusions not representative of the pre-solar composition. Since the half-life of ^{26}Al is 10^6 yr, the pre-solar enrichment in ^{26}Al suggests pollution by a nearby source of ^{26}Al, such as a supernova explosion (see Zinner et al. 1991; and Clayton 1994, for thorough discussions).

6. Conclusions

The VLT-UVES spectra of CH^+ absorption in the lines of sight toward 10 bright stars have allowed us to measure the carbon isotopic ratio $R = {}^{12}C/^{13}C$ with unprecedented accuracy. We confirm previous measurements of R toward ζOph, and obtain significant scatter in the local ISM.

Our value for ζOph is $R = 78.47 \pm 2.65(3.53)$, where the second uncertainty in parenthesis is that obtained a posteriori, from independent measurements, and independent baseline and absorption fits. Combining this value with that of Stahl et al. (1992) gives our best value for ζOph, $R = 74.7 \pm 2.3$.

Averaging our measurements for the 10 lines of sight gives a value representative of the local ISM: $\langle R_{\rm ISM}\rangle = 78.27 \pm 1.83$, with a weighted rms dispersion of 12.7. The dispersion in isotopic ratio is 7 times the uncertainty in $\langle R_{\rm ISM}\rangle$ – we detect heterogeneity at 7σ.

The observed scatter in $^{13}C/^{12}C$ is the first significant detection of heterogeneity in the isotopic composition of the local ISM, and was obtained with a single instrument and a homogeneous analysis, with a diagnostic independent of the local excitation and of chemical fractionation. The observed variations in R can be extrapolated to an overall elemental heterogeneity, and reveal that mixing in the ISM is not perfect.

The solar carbon isotope ratio of 90 is undistinguishable from the present-day ISM ratio, considering its intrinsic scatter, even after 4.5 Gyr of galactic evolution. This statement is not affected by instrumental uncertainties, although a sampling bias could distort our ISM value. We question whether the solar carbon isotopic ratio is equal to that of the presolar nebula.

A larger sample of stars, and new data towards the Pleiades, the Taurus cloud and P Cyg with 8 m aperture telescopes, will allow a better estimate of the average ISM value, and an improved understanding of the relationship between elemental heterogeneity and spatial scale in the ISM.

Acknowledgements. We thank the referee, Roland Gredel, for critical readings and constructive comments that improved the article. S.C. acknowledges support from Fondecyt grant 1030805, and from the Chilean Center for Astrophysics FONDAP 15010003.

References

Ayres, T. R., Plymate, C., Keller, C., & Kurucz, R. L. 2005, Eos. Trans. AGU, 86(18), Jt. Assem. Suppl., Abstract SP41B-09
Bruston, P., Audouze, J., Vidal-Madjar, A., & Laurent, C. 1981, ApJ, 243, 161
Casassus, S., & Roche, P. F. 2001, MNRAS, 320, 435
Centurion, M., & Vladilo, G. 1991, A&A, 251, 245
Centurion, M., Cassola, C., & Vladilo, G. 1995, A&A, 302, 243
Charbonneau, P. 1995, ApJS, 101, 309
Clayton, D. D. 1994, Nature, 368, 222
Crane, P., Hegyi, D. J., & Lambert, D. L. 1991, ApJ, 378, 181
Crane, P., Lambert, D., & Sheffer, Y. 1995, ApJS, 99, 107
Crawford, I. A. 1995, MNRAS, 277, 458
Crawford, I. A., Barlow, M. J., Diego, F., & Spyromilio, J. 1994, MNRAS, 266, 903
Draine, B. T. 2004, in Astrophysics in the Far Ultraviolet, ASP Conf. Ser. [arXiv:astro-ph/0410310]
Federman, S. R., Lambert, D. L., Sheffer, Y., et al. 2003, ApJ, 591, 986
Franco, G. A. P. 1989, A&A, 215, 119
Gredel, R., Van Dishoeck, E. F., & Black, J. H. 1993, A&A, 269, 477
Hawkins, I., & Jura, M. 1987, ApJ, 317, 926
Hawkins, I., & Meyer, D. M. 1989, ApJ, 338, 888
Hawkins, I., Jura, M., & Meyer, D. M. 1985, ApJ, 294, L131
Hawkins, I., Craig, N., & Meyer, D. M. 1993, ApJ, 407, 185
Jenkins, E. B., Tripp, T. M., Wozniak, P. A. R., Sofia, U. J., & Sonneborn, G. 1999, ApJ, 520, 182
Keene, J., Schilke, P., Kooi, J., et al. 1998, ApJ, 494, L107
Kirby, K., Roberge, W. G., Saxon, R. P., & Liu, B. 1980, ApJ, 239, 855
Moos, H. W., Sembach, K., Vidal-Madjar, A., et al. 2002, ApJS, 140, 3
Morton, D. C. 1975, ApJ, 197, 85
Murphy, D. C., Cohen, R., & May, J. 1986, A&A, 167, 234
Palla, F., Bachiller, R., Stanghellini, L., Tosi, M., & Galli, D. 2000, A&A, 355, 69
Prantzos, N. 2001, in Cosmic Evolution, ed. E. Vangioni-Flam, R. Ferlet, & M. Lemoine (New Jersey: World Sci. Publ.), 233
Press, H. W., Teukolsky, S. A., Vetterling, W. T., & Flannery, B. P. 1986, Numerical Recipes (Cambridge University Press)
Renzini, A., & Voli, M. 1981, A&A, 94, 175
Rosman, K. J. R., & Taylor, P. D. P. 1998, JPCRD, 27, 1275
Scalo, J., & Elmegreen, B. G. 2004, ARA&A, 42, 275
Sembach, K. R., & Savage, B. D. 1992, ApJS, 83, 147
Sheffer, Y., Federman, S. R., Lambert, D. L., & Cardelli, J. A. 1992, ApJ, 397, 482
Sonneborn, G., Tripp, T. M., Ferlet, R., et al. 2000, ApJ, 545, 277
Stahl, O., & Wilson, T. L. 1992, A&A, 254
Stahl, O., Wilson, T. L., Henkel, C., & Appenzeller, I. 1989, A&A, 221, 321
Stahl, O., Kaufer, A., & Tubbesing, S. 1999, in Optical and Infrared Spectroscopy of Circumstellar Matter, ASP Conf. Ser., 188, 331
Sternberg, A., & Dalgarno, A. 1995, ApJS, 99, 565
Tosi, M. 2000, in The Evolution of the Milky Way versus Star Clusters, ed. F. Matteucci, & F. Giovanelli (Dordrecht: Kluwer Publ.), 505
Vanden Bout, P. A., & Snell, R. L. 1980, ApJ, 236, 460
Vidal-Madjar, A. 2002, P&SS, 50, 1161
Vladilo, M., Centurion, M., & Cassola, C. 1993, A&A, 273, 239
Watson, W. D. 1978, ARA&A, 16, 585
Watson, W. D., Anicich, V. G., & Huntress, W. T., Jr. 1976, ApJ, 205, 165
Wielen, R. 1977, A&A, 60, 263
Wielen, R., & Wilson, T. L. 1997, A&A, 326, 139
Wilson, T. L., & Rood, R. T. 1994, ARA&A, 32, 191
Zinner, E., Amari, S., Anders, E., & Lewis, R. 1991, Nature, 349, 3

Online Material

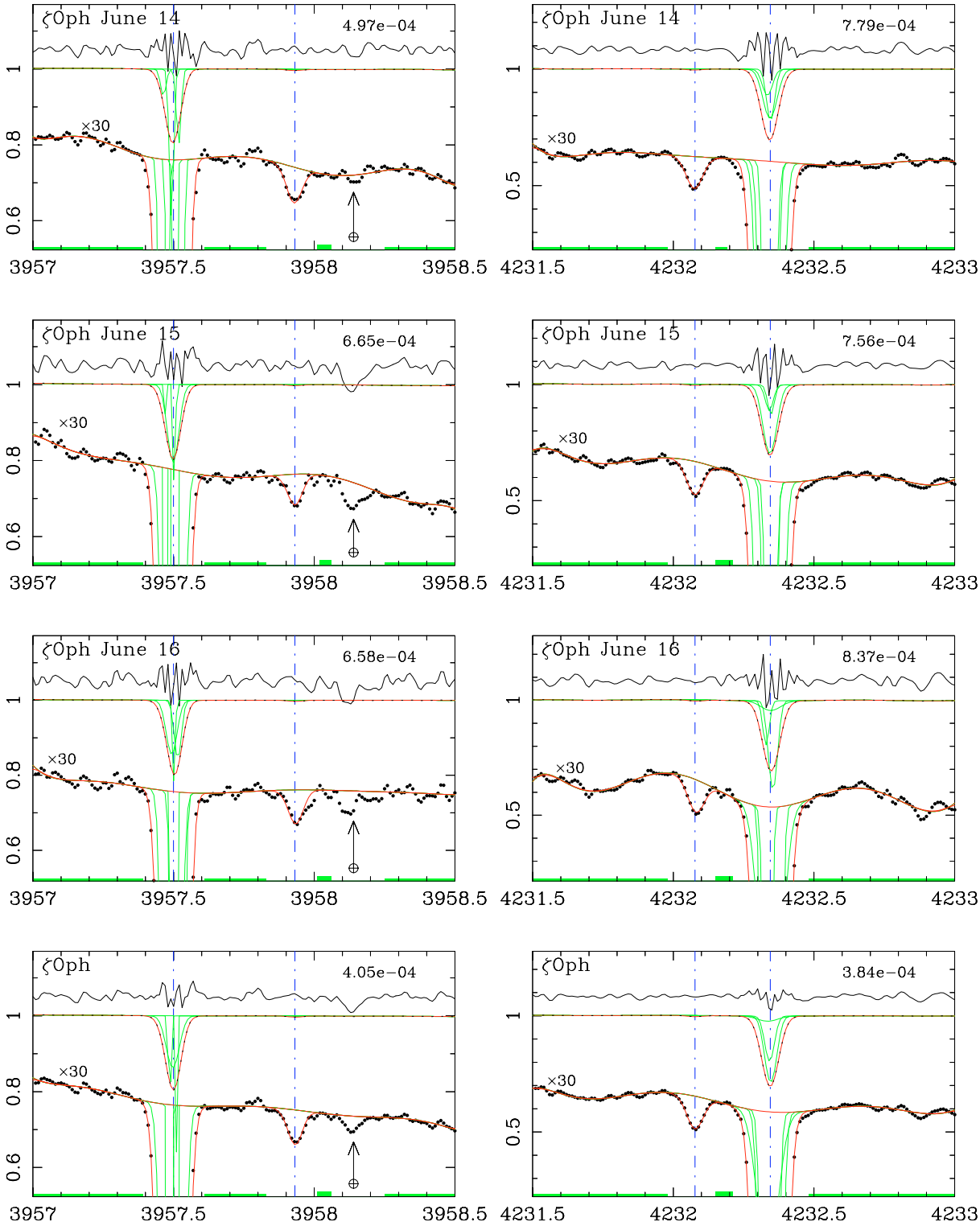

Fig. 3. ζOph spectra. Wavelengths are in Angstroms, and flux densities in arbitrary units. The individual Gaussian components comprising the fit, prior to folding with the instrumental response, are shown only on $^{12}CH^+$ as light gray lines, but are omitted from $^{13}CH^+$ for clarity (see text for details). The vertical dashed lines mark the line centroids, at the average of the Gaussian centroids weighted by their equivalent widths. The units of the *y*-axis are arbitrary, and are scaled so that the median of the object spectrum is unity. Also shown is a magnified version of the object spectrum, by the factor indicated on the figure, and offset for clarity. The residual spectrum is shown on top of the object spectrum, and is also magnified by the factor indicated on figure. The noise used to compute the significance of the fits is labelled on the top right. The noise is the rms dispersion of the residual spectrum, and is in the same units as the *y*-axis. The height of the shaded rectangles on top of the *x*-axis indicates the relative weights used in the baseline definition.

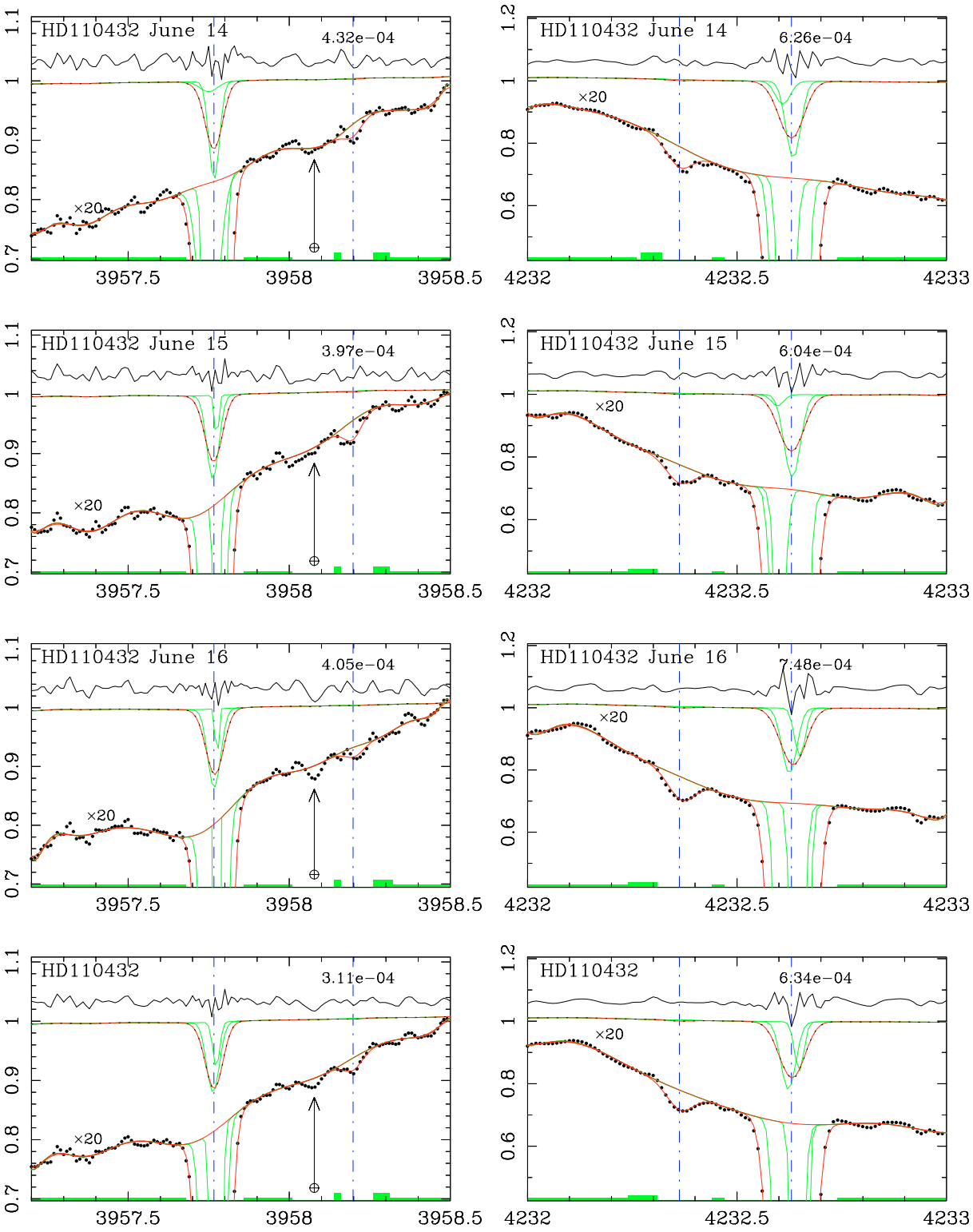

Fig. 4. Same as Fig. 3. The fits on the λ3957 lines are excluded from the combined measurement of R.

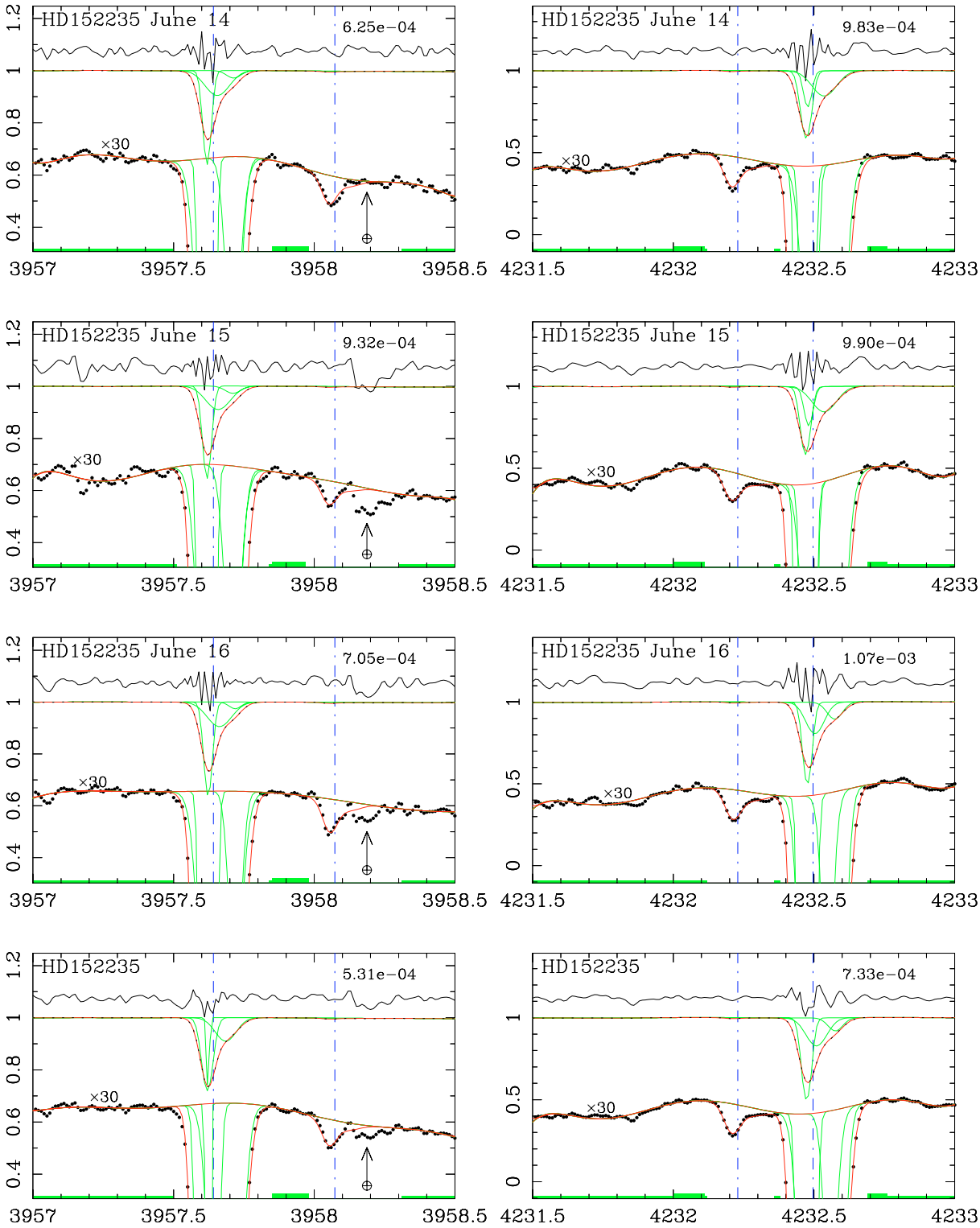

Fig. 5. Same as Fig. 3. The fits on λ3957 for June 15th and 16th are excluded from the combined measurement of R.

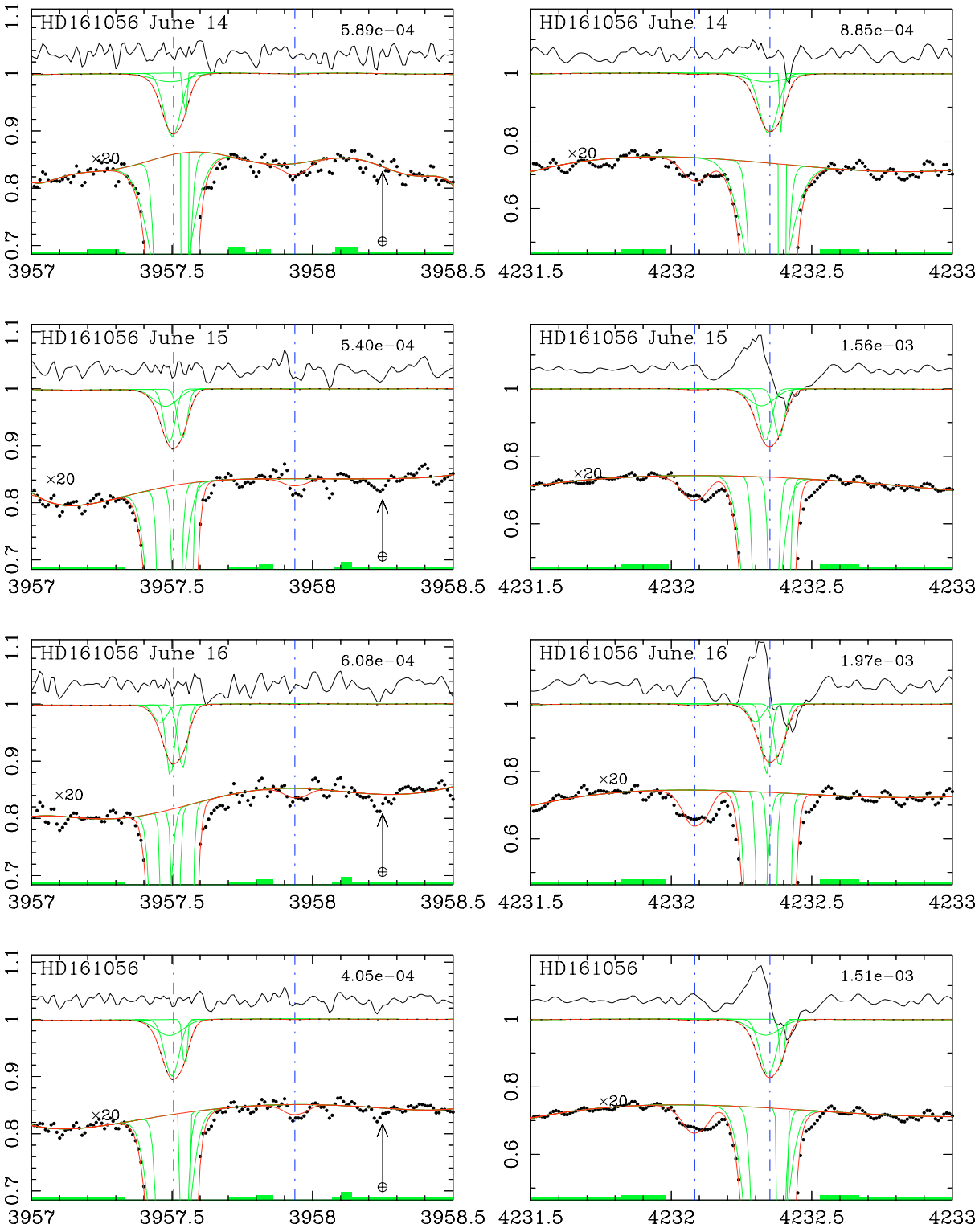

Fig. 10. Same as Fig. 3. None of the λ4232 spectra were used to combine individual measurements of R. There is excess absorption bridging the two isotopes at λ4232. The origin of the additional absorption, whether a telluric or a stellar feature, is unclear.

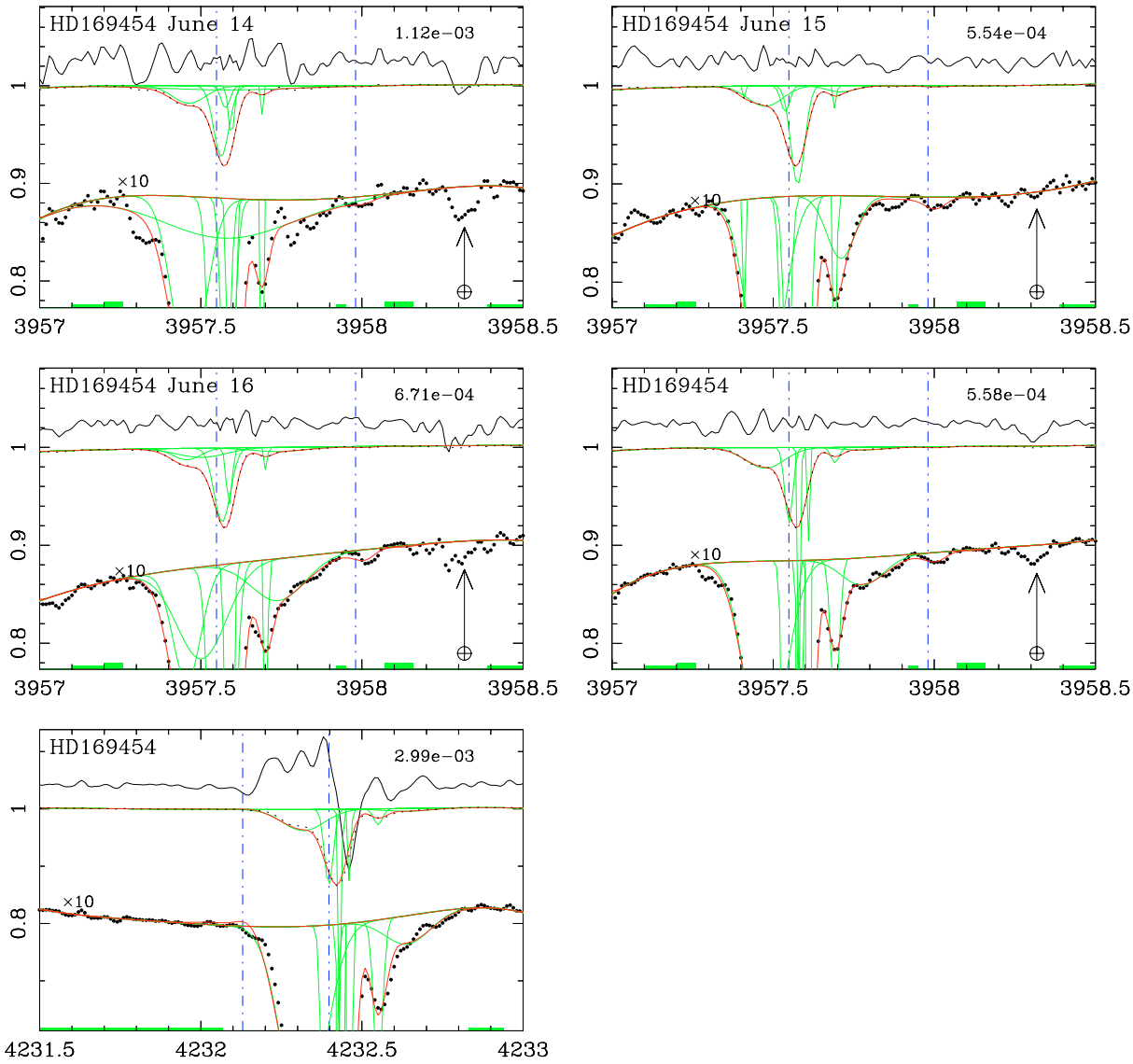

Fig. 11. Same as Fig. 8. The information from λ4232 is not used because f is spuriously negative, and neither is that from λ3957 on June 14th because of a non-ISM absorption feature at 3957.3 Å.

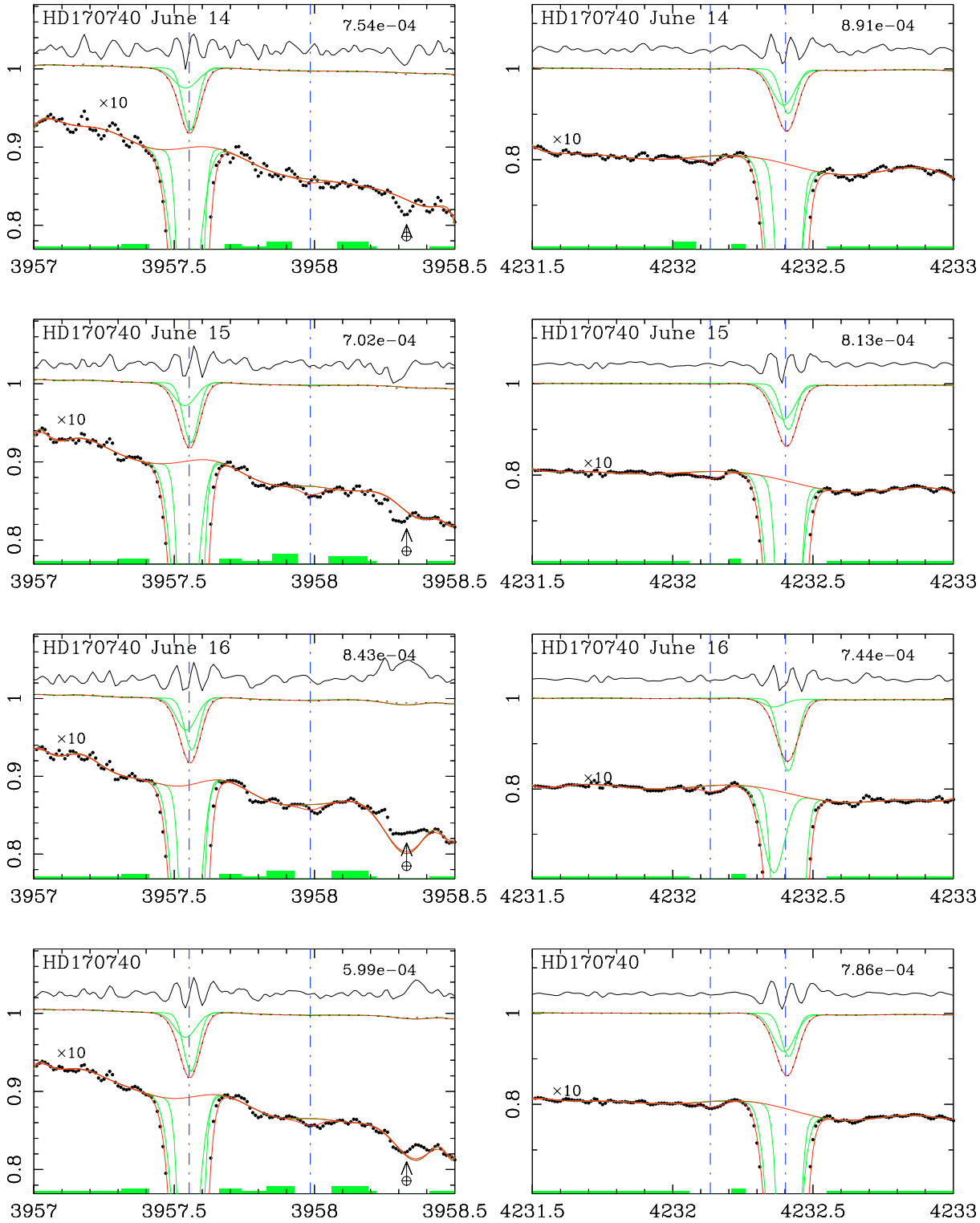

Fig. 12. Same as Fig. 8. The spectra around λ3957 have ragged baselines, presumably due to instrumental fringing. Only the coadded spectrum at λ3957 is used for subsequent averaging of R with that from λ4232.